

To appear in The Astronomical Journal (May 2002)

SPICES II. Optical and Near-Infrared Identifications of Faint X-Ray Sources from Deep *Chandra* Observations of Lynx¹

Daniel Stern², Paolo Tozzi^{3,4}, S. A. Stanford^{5,6}, Piero Rosati^{3,7}, Brad Holden^{5,6},
Peter Eisenhardt², Richard Elston⁸, K. L. Wu⁸, Andrew Connolly⁹,
Hyron Spinrad¹⁰, Steve Dawson¹⁰, Arjun Dey¹¹, & Frederic H. Chaffee¹²

ABSTRACT

We present our first results on field X-ray sources detected in a deep, 184.7 ks observation with the Advanced CCD Imaging Spectrometer (ACIS-I) on the *Chandra X-Ray Observatory*. The observations target the Lynx field ($\alpha_{J2000} = 08^h48^m$, $\delta_{J2000} = +44^\circ54'$) of SPICES, the Spectroscopic Photometric Infrared-Chosen Extragalactic Survey, which contains three known X-ray-emitting clusters at redshifts of $z = 0.57, 1.26$, and 1.27 . Not including the known clusters, in the $17' \times 17'$ ACIS-I field we detect

¹Some of the data presented herein were obtained at the W.M. Keck Observatory, which is operated as a scientific partnership among the California Institute of Technology, the University of California and the National Aeronautics and Space Administration. The Observatory was made possible by the generous financial support of the W.M. Keck Foundation. Based on observations with the NASA/ESA *Hubble Space Telescope*, obtained at the Space Telescope Science Institute, which is operated by the Association of Universities for Research in Astronomy, Inc. under NASA contract No. NAS5-26555. Based on observations at the Kitt Peak National Observatory, National Optical Astronomy Observatory, which is operated by the Association of Universities for Research in Astronomy, Inc. under cooperative agreement with the National Science Foundation.

²Jet Propulsion Laboratory, California Institute of Technology, Mail Stop 169-327, Pasadena, CA 91109 USA
[email: stern@zwozkinder.jpl.nasa.gov]

³Department of Physics and Astronomy, The Johns Hopkins University, Baltimore, MD 21218 USA

⁴Osservatorio Astronomico di Trieste, via G.B. Tiepolo 11, I-34131, Trieste, Italy

⁵Institute of Geophysics and Planetary Physics, Lawrence Livermore National Laboratory, L-413, Livermore, CA 94550 USA

⁶Physics Department, University of California at Davis, Davis, CA 95616 USA

⁷European Southern Observatory, Karl-Schwarzschildstr. 2, D-85748, Garching, Germany

⁸Department of Astronomy, University of Florida, P.O. Box 112055, Gainesville, FL 32611 USA

⁹Department of Physics and Astronomy, University of Pittsburgh, Pittsburgh, PA 15260 USA

¹⁰Department of Astronomy, University of California at Berkeley, Berkeley, CA 94720 USA

¹¹National Optical Astronomy Observatory, 950 North Cherry Avenue, Tucson, AZ 85719 USA

¹²W. M. Keck Observatory, 65-1120 Mamalahoa Highway, Kamuela, HI 96743 USA

132 sources in the 0.5–2 keV (soft) X-ray band down to a limiting flux of $\approx 1.7 \times 10^{-16} \text{ ergs cm}^{-2} \text{ s}^{-1}$ and 111 sources in the 2–10 keV (hard) X-ray band down to a limiting flux of $\approx 1.3 \times 10^{-15} \text{ ergs cm}^{-2} \text{ s}^{-1}$. The combined catalog contains a total of 153 sources, of which 42 are detected only in the soft band and 21 are detected only in the hard band. Confirming previous *Chandra* results, we find that the fainter sources have harder X-ray spectra, providing a consistent solution to the long-standing ‘spectral paradox’.

From deep optical and near-infrared follow-up data, 77% of the X-ray sources have optical counterparts to $I = 24$ and 71% of the X-ray sources have near-infrared counterparts to $K_s = 20$. Four of the 24 sources in the near-IR field are associated with extremely red objects (EROs; $I - K_s \geq 4$). We have obtained spectroscopic redshifts with the Keck telescopes of 18 of the Lynx *Chandra* sources. These sources comprise a mix of broad-lined active galaxies/quasars, apparently normal galaxies, and two late-type Galactic dwarfs. Intriguingly, one Galactic source is identified with an M7 dwarf exhibiting non-transient, hard X-ray emission.

Thirteen of the *Chandra* sources are located within regions for which we have *Hubble Space Telescope* imaging. Nine of the sources are detected, showing a range of morphologies: several show compact cores embedded within diffuse emission, while others are spatially extended showing typical galaxy morphologies. Two of the *Chandra* sources in this subsample appear to be associated with mergers.

We briefly review non-AGN mechanisms to produce X-ray emission and discuss properties of the Lynx *Chandra* sample in relation to other samples of X-ray and non-X-ray sources.

Subject headings: cosmology: observations – X-rays: galaxies – surveys – diffuse radiation – galaxies: active

1. Introduction

The launch of the *Chandra X-Ray Observatory* on 1999 July 23 opened a new era in our study of the X-ray universe. With its revolutionary mirror assembly design, *Chandra* provides $\approx 0''.5$ resolution imaging with $\approx 1''$ astrometry over the $\sim 0.1 - 10$ keV range (Weisskopf, O’deh, & van Speybroeck 1996). Furthermore, the deepest *Chandra* observations to date are ~ 50 times more sensitive than the deepest pre-*Chandra* observations in the 0.5 – 2 keV soft X-ray band (e.g., Hasinger et al. 1998) and more than two orders of magnitude more sensitive than the deepest pre-*Chandra* observations in the 2 – 10 keV hard X-ray band (e.g., Ueda et al. 1999; Fiore et al. 1999). At this resolution and depth, *Chandra* has resolved $> 90\%$ of the soft X-ray background and $\approx 80\%$ of the hard X-ray background into discrete sources (e.g., Mushotzky et al. 2000; Barger et al. 2001; Giacconi et al. 2001; Hornschemeier et al. 2001; Tozzi et al. 2001). *Chandra*’s imag-

ing resolution is also well-matched to the typical deep optical/near-infrared imaging resolutions, providing for the first time largely unambiguous identifications of the X-ray hosts. This affords an exciting new opportunity to study X-ray host identifications, thereby aiding our understanding of what powers the X-ray background. In particular, even heavily obscured active galactic nuclei (AGN) are expected to be luminous and largely unattenuated in the hard X-ray band: the great hope is that studying the resolved hard X-ray background can provide an unbiased picture of the history of accretion-driven energy production in the Universe.

With the goal of simultaneously studying both the X-ray background and the properties of intracluster media at high redshift, we obtained a deep, 184.7 ks exposure with the Advanced CCD Imaging Spectrometer (ACIS-I) on board *Chandra* of three spatially-proximate high-redshift galaxy clusters in the Lynx field of the SPICES survey (Eisenhardt et al. 2001, see §4 below). All three clusters were identified in the *ROSAT* Deep Cluster Survey (RDCS; Rosati et al. 1995, 1998) and reside within a single ACIS-I field. Two are at $z > 1$, among the most distant X-ray-emitting galaxy clusters known: RX 0848+4453 at $z = 1.27$ (Stanford et al. 1997) and RX 0849+4452 at $z = 1.26$ (Rosati et al. 1999). The third cluster is at $z = 0.57$ (RX 0848+4456; Rosati et al. 1998). At 184.7 ks, our *Chandra* observation is among the deepest observations of the X-ray sky taken to date. Analysis of the diffuse X-ray emission from the intracluster media of the two $z > 1$ clusters is presented in Stanford et al. (2001) and suggests little evolution in the X-ray luminosity – temperature ($L_X - T_X$) relation to $z \approx 1.3$. Analysis of the diffuse X-ray emission from the $z = 0.570$ cluster is presented in Holden et al. (2001) and suggests that 10–20% of the X-ray emission actually comes from a group at $z = 0.543$ along the line of sight, showing the importance of detailed and multiwavelength studies of galaxy clusters when using them as probes of cosmological mass functions. Observations of the 153 X-ray point sources are the subject of the remainder of this paper.

To aid in follow-up observations, this manuscript details and provides a catalog of the unresolved X-ray sources we identify from the deep $17' \times 17'$ ACIS-I image (§ 2). In § 3 we discuss results from the X-ray data alone, including the hardness ratio and the fraction of the X-ray background which is resolved from these observations. SPICES optical (*BRIz*) images cover the central $16' \times 16'$ of this field and SPICES near-infrared (*JK_s*) images cover the central $5.6' \times 5.6'$ of this field: we present the results of our cross-correlation of the optical/near-infrared imaging data with the X-ray catalog in § 4. The 18 redshifts we have obtained for Lynx *Chandra* sources are also discussed in § 4. Section 5 presents our first spectroscopic results and § 6 highlights some initial results from this work. We summarize our conclusions in § 7. An additional, interesting X-ray source in this field, CXO52, is the subject of Stern et al. (2002). Unless otherwise stated, all magnitudes presented are in the Vega system. Cosmology-dependent parameters are calculated for two models: an Einstein-de Sitter universe consistent with previous work in this field ($H_0 = 50 h_{50} \text{ km s}^{-1} \text{ Mpc}^{-1}$, $\Omega_M = 1$, and $\Omega_\Lambda = 0$) and the dark energy universe favored by recent work on high-redshift supernovae and fluctuations in the cosmic microwave background ($H_0 = 65 \text{ km s}^{-1} \text{ Mpc}^{-1}$, $\Omega_M = 0.35$, and $\Omega_\Lambda = 0.65$; e.g., Riess et al. 2001).

2. X-Ray Data: Observations and Source Detection

2.1. Observations and data reduction

ACIS-I observations of the Lynx field were obtained on 2000 May 3 (65 ks; OBS-ID 1708) and 2000 May 4 (125 ks; OBS-ID 927). The aimpoint for the observations was $\alpha_{J2000} = 08^h48^m54.79^s$, $\delta_{J2000} = +44^\circ54'32''.9$ and both exposures were obtained in the faint mode when ACIS was at a temperature of -120° C. The Galactic absorbing column for this field is $N_H = 2 \times 10^{20} \text{ cm}^{-2}$. The position angle of the observations was 258.45° .

The data were reduced and analyzed using the *Chandra* Interactive Analysis of Observations (CIAO) software (release V1.1, see <http://asc.harvard.edu/ciao>). The Level 1 data were processed using the quantum efficiency uniformity file for -120° C, which corrects the effective area for loss due to charge transfer inefficiency. The correction compensates for the loss of events far from the readout, especially at high energies, and is relevant when fitting the total spectrum in the largest energy range. The data were filtered to include only the standard event grades 0, 2, 3, 4, and 6. All bad columns were removed by eye, as were the columns close to the border of each node, since the grade filtering is not efficient in these columns. We also identified flickering pixels in the images in the chip coordinates: for each chip, we checked photon arrival times for all pixels on which more than two photons were detected. If two or more photons were detected within an interval shorter than 7 seconds, they were considered flickering pixels and excluded from further analysis. As the brightest source (CXO39) has a count rate of only 1 photon every ≈ 100 seconds, this procedure should not affect our source catalog. The removal of columns and pixels reduces slightly the effective area of the detector, the result of which has been included when calculating the soft and hard exposure maps.

Time intervals with background rates larger than 3σ over the quiescent value ($\simeq 0.30 \text{ counts s}^{-1}$ per chip in the $0.3 - 10 \text{ keV}$ band) were removed. This procedure gave 60.7 ks of effective exposure out of the first observation, and 124 ks out of the second, for a total of 184.7 ks. The two observations are almost coincident on the sky, so that the total coverage is 298 arcmin^2 . The two event files were merged into a single file, which was used in the reduction and analysis process. The astrometry of the two observations, contiguous in time, was perfectly consistent, as verified by registering the positions of the brightest sources on top of each other. We did not include data from the chips S-2 and S-3 in the following analysis, since the point spread function (PSF) is very broadened ($\simeq 15 \text{ arcsec}$) and they would add a very little effective area even for high fluxes. Fig. 1 shows the final, combined X-ray data, with a false-color mapping derived from the *Chandra* energy bands.

2.2. Source detection

A soft band from 0.5–2 keV and a hard band from 2–7 keV were used in the detection process to select a soft and hard source lists, as detailed below. The hard band detection window was cut at 7 keV since above this energy the effective area of *Chandra* is decreasing, while the instrumental background is rising, giving very inefficient detection of sky photons. X-ray count rates in the above bands were used to calculate X-ray fluxes in a 0.5–2 keV soft band and 2–10 keV hard band, assuming an average X-ray spectrum.

We ran Source Extractor (Bertin & Arnouts 1996) on the summed 0.5–7 keV image binned by a factor of two (one binned pixel corresponds to $0.982'' \times 0.982''$). Since we are far from being background limited, the detection efficiency proved to be much higher for the 0.5–7 keV image rather than the soft and hard bands separately. Giacconi et al. (2001) use the same procedure for their analysis of the *Chandra* Deep Field-South (CDF-S). Source Extractor parameters were chosen after extensive simulations, and we adopted an internal detection threshold signal-to-noise (S/N) ratio of 2.4, with a Gaussian filter FWHM of $1''.5$ and a minimum area of 5 pixels. Since Source Extractor is not tailored to work with a very low background, it gives a wrong estimate of the internal background. To tackle this problem, we built a smoothed map of the background computed from the data themselves in the corresponding band, after the removal of the sources down to a very low threshold. This background map was used as a weight (variance) map to define the detection threshold. This modified detection algorithm is several orders of magnitude faster than the wavelet detection algorithm of Rosati et al. (1995) or the WAVDETECT algorithm in the CIAO software (Freeman et al. 2002).

Table 1 presents the catalog of 0.5 – 7 keV point sources identified in the combined image, selected as follows. We first measured the signal-to-noise (S/N) ratio of all the candidate detections in circular extraction apertures. A radius $R_S = 2.4 \times \text{FWHM}_{\text{PSF}}$ was used, where FWHM_{PSF} is the modeled PSF full-width at half-maximum, determined as a function of off-axis angle to reproduce the broadening of the PSF. A minimum $R_S = 5''$ was used in the central regions. Sources with $S/N > 2.1$ within the extraction area were considered detections. This limit was chosen to provide a census of X-ray sources to faint flux levels, where the choice of Source Extractor parameters has already significantly reduced the number of spurious detections. We stress as a compromise between providing a census of X-ray sources to faint levels and limiting the contamination from false detections. We stress that the condition of having $S/N > 2.1$ in the extraction area corresponds to a high significance detection – the faintest detected sources have more than 10 counts. These catalogs, obtained from the Source Extractor run and the a-posteriori S/N cut, typically include less than five spurious sources as tested with simulations with the Model of *AXAF*¹³ Response to X-rays (MARX) software (for a detailed description of the simulations, see Tozzi et al. 2001). After performing this procedure on the soft and hard images separately, we obtained the soft and hard catalogs. A combined catalog was then produced by matching the two. Source counts were measured with simple aperture photometry within R_S . The background for each source was calculated locally within an annulus of inner radius $R_S + 2''$ and an outer radius of $R_S + 12''$.

Numerical simulations show that our aperture photometry systematically underestimates the net counts by 4%. For the following analysis, we have applied this aperture correction.

Finally, we transformed the net count rate into energy flux in the soft 0.5–2 keV band and in the hard 2–10 keV band. The conversion factors used were $(4.52 \pm 0.3) \times 10^{-12}$ erg cm⁻² count⁻¹ in the soft band and $(2.79 \pm 0.3) \times 10^{-11}$ erg cm⁻² count⁻¹ in the hard band, assuming an absorbing column of 2×10^{20} cm⁻² (Galactic value) and a photon index¹⁴ $\Gamma = 1.4$. The uncertainties in the conversion factors reflect the range of possible values for the photon index, $\Gamma = 1.1 - 1.8$. As suggested by the spectral analysis of the stacked spectra, these values are representative of our sample (see below). Since the conversion factors were computed at the aimpoint, where the effective area of *Chandra*/ACIS is at its maximum, the count rate of each source was corrected for vignetting. Namely, the net count rate was multiplied by the ratio of the exposure map at the aimpoint to the value of the exposure map averaged within the extraction region. Such a correction was done in the soft and hard bands separately.

We detect 132 sources in the 0.5–2 keV (soft) X-ray band down to a 2.1σ limiting flux of $S_{0.5-2} \approx 1.7 \times 10^{-16}$ ergs cm⁻² s⁻¹ and 111 sources in the 2–10 keV (hard) X-ray band down to a 2.1σ limiting flux of $S_{2-10} \approx 1.3 \times 10^{-15}$ ergs cm⁻² s⁻¹. Only the point sources are considered here. As mentioned above, the diffuse galaxy cluster emissions are explored by Stanford et al. (2001) and Holden et al. (2001). Of the total catalog of 153 sources, 42 (27%) are detected only in the soft band and 21 (14%) are detected only in the hard band. These results are very similar to the fractions derived by Tozzi et al. (2001) for their 300 ks ACIS map of the CDF-S: referred to the total sample, they find 26% of the sources are detected only in the soft band and 11% of the sources are detected only in the hard band.

Astrometric positions were initially determined from the ACIS-I aspect solution. Following comparison of X-ray source positions to the deep, ground-based imaging discussed in §4, we refined the absolute pointing of the X-ray data with an offset of 1''09 west, 1''35 south, and no rotation. These offsets were determined by matching X-ray sources with greater than 25 total counts (0.5 – 7 keV) to $17.5 < I < 22.5$ sources. The positions presented in Table 2 therefore match the astrometric frame of the SPICES survey.

3. X-Ray Data: Results

¹³The *Chandra X-ray Observatory* was formerly known as *AXAF*, the *Advanced X-ray Astrophysics Facility*.

¹⁴The number of X-ray photons $N(E)$ detected as a function of energy E is assumed to follow a power law distribution, $N(E)dE \propto E^{-\Gamma}dE$, where Γ is the photon index.

3.1. Resolving the X-ray background

To compute the number counts in the soft and hard bands, we first calculate the sky coverage as a function of the flux. The effective sky coverage of a given flux is defined as the area on the sky where a soft (or hard) source can be detected with a $S/N > 2.1$ in the extraction region defined above. We have performed extensive simulations with MARX to show this procedure is accurate within a few percent (e.g., see Tozzi et al. 2001). The same procedure has been used for the CDF-S (Giacconi et al. 2001).

In Fig. 2 we present the soft X-ray source counts derived from our observations. For comparison, we also show source counts from the deep *ROSAT* observations of the Lockman Hole (Hasinger et al. 1998), extrapolation of the source counts to fainter fluxes from fluctuation analysis of the *ROSAT* data (Hasinger et al. 1993), and recent, deep *Chandra* soft X-ray source counts from Mushotzky et al. (2000). We find the *Chandra* results in excellent agreement with *ROSAT* in the region of overlap $S_{0.5-2} > 10^{-15}$ ergs cm $^{-2}$ s $^{-1}$. The *Chandra* data extend the results to 2×10^{-16} ergs cm $^{-2}$ s $^{-1}$. A maximum-likelihood power-law fit to the soft X-ray $\log N - \log S$ data finds

$$N(> S_{0.5-2}) = 320 \pm 80 \left(\frac{S_{0.5-2}}{2 \times 10^{-15} \text{ ergs cm}^{-2} \text{ s}^{-1}} \right)^{-0.82 \pm 0.10}.$$

Confidence contours for the slope and the normalization of the soft counts are shown in the upper right corner of Fig. 2, compared with the results of Mushotzky et al. (2000). Note that here we used an average slope to be consistent with the average spectrum of our sample of sources.

In Fig. 3 we present the hard X-ray source counts derived from our observations down to a flux limit of 2×10^{-15} ergs cm $^{-2}$ s $^{-1}$. At bright levels source counts from the *Advanced Satellite for Cosmology and Astrophysics* (*ASCA*) and *BeppoSAX* are shown (Giommi et al. 1998; della Ceca et al. 1999; Ueda et al. 1999). At faint levels we show recent, deep *Chandra* hard X-ray source counts from Mushotzky et al. (2000). A maximum-likelihood power-law fit to the hard X-ray $\log N - \log S$ data finds

$$N(> S_{2-10}) = 1400 \pm 200 \left(\frac{S_{2-10}}{2 \times 10^{-15} \text{ ergs cm}^{-2} \text{ s}^{-1}} \right)^{-1.12 \pm 0.17}.$$

Confidence contours are again provided, as per Fig. 2. Our hard-band $\log N - \log S$ results are consistent with deep observations of the Lockman Hole obtained with the *X-Ray Multi-Mirror-Newton* satellite (*XMM-Newton*; Hasinger et al. 2001). Our normalization of the hard-band $\log N - \log S$ relation is 1σ higher than the results for the CDF-S who find a normalization to the above relation of $K_{15} = 1150 \pm 150$ where $N(> S_{2-10}) = K_{15}(S_{2-10}/2 \times 10^{-15} \text{ ergs cm}^{-2} \text{ s}^{-1})^{-\alpha}$ (Tozzi et al. 2001). In both the soft and the hard X-ray bands, the Lynx-field source counts are slightly lower at each X-ray flux than those determined for SSA13 (Mushotzky et al. 2000). The difference likely reflects cosmic variance due to large scale structure on size scales similar to the *Chandra* field-of-view. In particular, the SSA13 results analyze only one ACIS chip, thus sampling one-quarter the area of the results discussed here. We note that four of the deepest $16' \times 16'$ *Chandra* fields

(CDF-S, HDF-N, the Lockman Hole, and Lynx) find consistent normalizations to the $\log N - \log S$ relation, while SSA13 and the MS1137 fields give 40% higher normalizations (Tozzi, in preparation)

What fraction of the hard X-ray background is resolved by the deep Lynx *Chandra* map? Fig. 4 presents the integrated contribution of resolved hard X-ray sources as a function of X-ray flux. In the range $(1 - 100) \times 10^{-15} \text{ ergs cm}^{-2} \text{ s}^{-1}$, the integrated hard X-ray flux density in the 2–10 keV band is $(1.2 - 1.3 \pm 0.1) \times 10^{-11} \text{ ergs cm}^{-2} \text{ s}^{-1} \text{ deg}^{-2}$, depending on the assumed average power law ($\Gamma = 1.6 - 1.4$, respectively). Including the hard-band $\log N - \log S$ relation derived by della Ceca et al. (1999) for a wider-area, brighter *ASCA* survey, we find that $(1.5 \pm 0.2) \times 10^{-11} \text{ ergs cm}^{-2} \text{ s}^{-1} \text{ deg}^{-2}$ of the hard X-ray background is resolved to a flux limit of $10^{-15} \text{ ergs cm}^{-2} \text{ s}^{-1}$. As seen in Fig. 4, this is close to the *High Energy Astronomy Observatory-1* (*HEAO-1*) value of $1.6 \times 10^{-11} \text{ ergs cm}^{-2} \text{ s}^{-1} \text{ deg}^{-2}$ (Marshall et al. 1980), but 20 – 40% lower than the more recent determinations from *BeppoSAX* and *ASCA* (e.g., Vecchi et al. 1999; Ishisaki et al. 1999). For comparison, from the first 300 ks observation of the CDF-S, Tozzi et al. (2001) resolve $(1.45 \pm 0.15) \times 10^{-11} \text{ ergs cm}^{-2} \text{ s}^{-1} \text{ deg}^{-2}$ of the hard X-ray background while Mushotzky et al. (2000) resolve $\approx 1.8 \times 10^{-11} \text{ ergs cm}^{-2} \text{ s}^{-1} \text{ deg}^{-2}$ in their 101 ks observation of SSA13. We conclude that, given the uncertainty on the value of the total background, a fraction between 20% and 40% of the hard X-ray background is still unresolved in our data set.

3.2. Hardness ratio

A long-standing problem in X-ray astrophysics has been that the spectral slope of the X-ray background is significantly steeper than the spectral slopes of the first (brightest) soft X-ray sources which were identified. The majority of these bright sources are identified with unobscured AGN (e.g., Schmidt et al. 1998). This problem, the so-called “spectral paradox,” implies that a new population of fainter sources with harder X-ray indices exists: obscured AGN are the likely culprit. *Chandra* has now identified this population.

Fig. 5 illustrates the hardness ratio $HR \equiv (H - S)/(H + S)$ for the Lynx sample, where H and S are the net counts in the hard (2 – 7 keV) and soft (0.5 – 2 keV) bands, respectively. The hardness ratio is plotted against the hard X-ray flux. There are 21 sources, corresponding to 14% of the total combined sample, which are detected only in the hard band (plotted at $HR = 1$) and 42 which are detected only in the soft band (not plotted). A population of hard sources, largely absent at bright fluxes, clearly emerges at faint fluxes. These results are analogous with the ones found in the CDF-S (Giacconi et al. 2001). We note that in the Lynx field there are three bright outliers in the hardness ratio–flux plane, in the upper right corner. These are very absorbed sources ($10^{22} < N_H < 10^{23} \text{ cm}^2$). In particular, the brightest one, CXO12, dominates the spectrum of the bright end of our sample, giving an effective $\Gamma \simeq 1.3$ already for fluxes $S_{2-10} \simeq 10^{-13} \text{ erg cm}^{-2} \text{ s}^{-1}$. CXO12 is identified with the $z = 0.9$ Type 2 quasar AX J08494+4454 reported by Ohta et al. (1996) and Nakanishi et al. (2000) from *ASCA* observations of the Lynx field. Of the other two hard, bright X-ray sources which stand out in Fig. 5, only one (CXO36) is within the area imaged

optically in the current work. Optical spectra from these other two sources are not discussed in the current work.

Fig. 6 presents the average spectral index of the population, determined from the stacked spectrum of all 154 sources in the combined sample. As a background, we used the stacked spectrum of all the background regions extracted around each source. The resulting photon files were scaled by the ratio of the total area of extraction of the sources and the corresponding area for the background. This procedure guarantees a correct background subtraction despite the non-uniformities of the instrumental background across ACIS-I. The response matrices for the stacked spectra were obtained from the counts-weighted average of the matrices for individual sources. XSPEC, the X-ray spectral fitting package (Arnaud 1996), was used to compute the slope of a power law spectrum with local N_H absorption in the energy range 0.5 – 7 keV. We excluded bins below 0.5 keV because the calibration is still uncertain below this energy. We obtained a photon index Γ of 1.36 ± 0.04 and a column density $N_H = (2.3 \pm 1.4) \times 10^{20} \text{ cm}^{-2}$ which is consistent with the Galactic value (errors refer to the 90% confidence level). The results of the spectral fits are shown in Fig. 6. We find an average spectrum for the detected sources is consistent with the average shape of the hard background ($\langle \Gamma \rangle \simeq 1.4$).

4. Optical/Near-Infrared Imaging

4.1. Summary of survey observations

The Lynx field is one of four fields which comprise SPICES (Eisenhardt et al. 2001). This long-term project was conceived as the next generation analog to the *I*-selected Canada-France Redshift Survey (CFRS; Lilly et al. 1996): by studying a sample of *K*-selected faint field galaxies over a larger, 100 arcmin² field, we are attempting to address the history of galaxy formation and evolution out to $z \simeq 1.5 - 2$ in a manner which is less-biased by large scale structure and recent star formation. In particular, selecting galaxies at $2\mu\text{m}$ should essentially translate to selecting by mass, thereby providing a powerful discriminant of theories of galaxy assembly (e.g., Kauffmann & Charlot 1998). Four unremarkable but well-studied fields were chosen spread across the sky for efficient follow-up throughout the year. Details of the motivation and imaging observations are presented in Eisenhardt et al. (2001). We briefly summarize the Lynx observations here.

Optical *BRIz* imaging was obtained using the Kitt Peak National Observatory 4 m Mayall telescope with its Prime Focus CCD imager (PFCCD) equipped with a thinned AR coated 2048 × 2048 Tektronics CCD. This configuration gives a $16' \times 16'$ field of view with $0''.47 \text{ pix}^{-1}$. The filters used were a Harris *B*-band ($\lambda_c = 4313 \text{ \AA}$; $\Delta\lambda = 1069 \text{ \AA}$), Harris *R*-band ($\lambda_c = 6458 \text{ \AA}$; $\Delta\lambda = 1472 \text{ \AA}$), Harris *I*-band ($\lambda_c = 8204 \text{ \AA}$; $\Delta\lambda = 1821 \text{ \AA}$), and an RG850 long-pass *z*-band filter. For the *I* and *z* imaging, the CCD was operated using “short scan,” where the CCD was mechanically displaced while its charge is shifted in the opposite direction to reduce fringing to very low levels. The combined, processed images reach limiting Vega magnitudes of 26.9 (*B*), 25.4 (*R*), 24.6 (*I*),

and 24.2 (z), where these numbers represent 3σ limits in $3''$ diameter apertures. The corresponding AB magnitude limits are 26.8, 25.6, 25.1, and 24.7, respectively. The seeing for the summed images ranges from $1''.2$ (B) to $1''.0$ (z). Data reduction followed standard techniques (for details, see Eisenhardt et al. 2001).

Near-infrared JK_s imaging was obtained at the KPNO 4 m with its Infrared Imager (IRIM; Fowler et al. 1988) equipped with a Rockwell International NICMOS 3 256×256 HeCdTe array giving $0''.6 \text{ pix}^{-1}$. Four pointings were obtained to cover a $5'.6 \times 5'.6$ area. The average exposure time in the fully sampled regions of the resulting mosaic was 10.14 ks in J ($\lambda_c = 1.14\mu\text{m}$; $\Delta\lambda = 0.29\mu\text{m}$) and 8.49 ks in K_s ($\lambda_c = 2.16\mu\text{m}$; $\Delta\lambda = 0.33\mu\text{m}$). The seeing in the mosaics is $1''.2 - 1''.3$. Data reduction followed standard techniques (for details, see Eisenhardt et al. 2001). Calibrations of the optical and near-infrared images onto the Landolt and CIT systems were obtained using observations of Landolt (1992) and UKIRT standard stars (Hawarden et al. 2001), respectively. The J -band images reach a 3σ limiting magnitude of 22.9 (Vega) in a $3''$ diameter aperture. The corresponding depth for the K_s images is $K_s = 21.4$.

We used Source Extractor (release V2.1.6; Bertin & Arnouts 1996) to create independent catalogs of sources selected from the B -, I -, and K_s -band images. Photometry was generated for $3''.0$ diameter apertures and evaluated in the same apertures for all six coaligned bands.

4.2. Optical/near-infrared counterparts

Fig. 7 shows the X-ray-to-optical positional offsets after the X-ray positions have been shifted by $1''.09$ west and $1''.35$ south (see §2.2). Based on these results, we matched the optical/near-infrared and X-ray source catalogs using a $1''.5$ radius aperture for host identification. Table 2 presents the optical/near-infrared properties of the *Chandra* sources listed in Table 1. As indicated in the table, for some sources, primarily fainter X-ray sources for which the X-ray position is more uncertain, we have used a larger ($1''.5 - 2''.3$) match radius. Non-detections are listed with an ellipsis (“...”) while sources with bad photometry, due either to source saturation or contamination from the stellar bleed trail of a nearby, bright source, are listed as 99.00. Only those sources within the smaller near-infrared field are tabulated in the near-infrared photometry columns. Sources from Table 1 not within the optical field are not included in Table 2. Only 104 of the X-ray sources are within the optical image field of view. Of these, 80, or 77%, have $I < 24$ (Vega) identifications. The infrared field of view covers 24 of the X-ray sources, of which 17, or 71%, have $K_s < 20$ (Vega) identifications. When we restrict ourselves to *Chandra* sources with signal-to-noise ratios greater than 3, the absolute numbers of X-ray sources in each region drops by $\sim 30\%$ but the fraction of sources with I and/or K_s identifications does not change substantially.

From the SPICES imaging we find that the surface density of sources to $K_s = 20$ is $\approx 15 \text{ arcmin}^{-2}$, so the probability of a chance coincidence of an X-ray source within $1''.5$ of a $K_s \leq 20$ source is $\approx 3\%$. We therefore expect none of the 17 $K < 20$ identifications to be spurious.

The surface density of $I < 24$ (Vega) sources is $\approx 23.5 \text{ arcmin}^{-2}$ so the probability of a chance juxtaposition of an X-ray source with an $I \leq 24$ source with our $1''.5$ match radius is $\approx 5\%$. We therefore expect that up to five of the faint host identifications in Table 2 to be spurious. Note that most of the optical identifications are in fact much brighter than $I = 24$, and are thus less likely to be spurious.

In Fig. 8 we present color-magnitude diagrams for sources detected in our near-infrared imaging field. X-ray sources are indicated with larger symbols. We see that for a given optical magnitude, the X-ray source hosts tend to be red in optical-to-near-IR color, hugging the so-called *red envelope*. Several of these sources meet the standard identity criteria of extremely red objects (EROs; e.g., Graham & Dey 1996): one source has $R - K > 6$ and four sources have $I - K > 4$. We know from previous X-ray surveys that many bright, early-type galaxies at moderate redshift are X-ray luminous; *Chandra*-identified EROs may represent the higher-redshift tail of that population. Indeed, Cowie et al. (2001) suggest that identifying optically-faint, hard X-ray sources may prove an efficient strategy to locate luminous, evolved galaxies at high redshift ($z \gtrsim 1.4$). We note that optically-faint, *soft* X-ray sources are also occasionally identified with high-redshift, early-type galaxies (e.g., CXO138; § 6.4.2). Highly-obscured sources are also expected to have red colors and may represent some fraction of extremely red X-ray sources. Contrary to that expectation, the $z = 3.70$ Type II quasar in the CDF-S identified by Norman et al. (2001) is relatively blue in optical-to-near-IR color: $R - K = 2.56$ and $I - K = 1.68$. A smaller subset of the X-ray sources have identifications which have blue optical-to-near-IR colors. These sources tend to be associated with broad-lined, bright quasars.

4.3. *Hubble Space Telescope* morphologies

Thirteen of the *Chandra* sources in the Lynx field are located in regions for which we have images from the Wide Field Planetary Camera 2 (WFPC2; Trauger et al. 1994) on the *Hubble Space Telescope* (*HST*; Fig. 9). These observations, sampling several independent observing programs, primarily target galaxy clusters in the Lynx field and range from 2 to 10 orbits (4.8 to 27 ks) through the F702W (12 ks; RX J0848+4456 region) and F814W (all other imaging) filters. The observations are described in van Dokkum et al. (2001), Holden et al. (2001), and Wu et al. (in preparation).

Only nine (69%) of the sources are detected in the *HST* images, lower than expected for a larger sample given that 77% of the full catalog have $I < 24$ identifications. This fraction is also lower than the 92% of CDF-S X-ray sources with optical counterparts in the deeper *HST*/WFPC2 study of Schreier et al. (2001), which reaches a detection limit of $I = 28.2$. Of the four Lynx non-detections (CXO46, CXO127, CXO135, and CXO136), three are detected in the X-ray with signal-to-noise ratios $S/N \leq 3$. The nine detections show a range of morphology. CXO42 and CXO49 are unresolved spatially, though both show faint, surrounding diffuse emission. CXO41 also has a very strong core, embedded in extended emission suggestive of a tidal tail or spiral

arm. CXO44 and CXO124 also appear to be associated with merging systems, while the remaining sources (CXO52, CXO60, CXO122, and CXO205) are spatially extended. The faint, soft X-ray source CXO205 appears to be associated with an early-type galaxy.

4.4. X-ray-to-optical flux ratio

Fig. 10 illustrates the X-ray-to-optical flux ratio of soft and hard X-ray sources. Following Hornschemeier et al. (2001), we plot lines of constant X-ray-to-optical flux ratio using the relation

$$\log \left(\frac{f_x}{f_R} \right) = \log f_x + \frac{R}{2.5} + 5.50,$$

derived from the Kron-Cousins R -band filter transmission function. At bright X-ray fluxes, we plot the results of shallow, wide-area surveys: for soft X-rays, we show AGN from the *ROSAT* survey reported by Schmidt et al. (1998) and for hard X-rays, we show sources from the *ASCA* survey reported by Akiyama et al. (2000). At faint X-ray fluxes we show the results of the *Chandra* Lynx survey reported here and results from the 221.9 ks *Chandra* study of the *Hubble* Deep Field North (HDF-N) reported in Hornschemeier et al. (2001). The majority of sources have $-1 \lesssim \log(f_x/f_R) \lesssim 1$, which, as we see from the shallow surveys, is typical of AGN. However, at the fainter fluxes probed by *Chandra*, new populations become apparent.

At faint, soft X-ray fluxes, several sources are seen which are X-ray underluminous for their optical magnitudes. Optical spectroscopy (see §5 and Hornschemeier et al. 2001; Tozzi et al. 2001) reveal many of these sources to be apparently normal galaxies. We discuss these sources further in §6.4. Several Galactic M dwarfs are also identified with $\log(f_x/f_R) \approx -2$, discussed further in §6.3. We note that one late-type Galactic dwarf has been identified in the Lynx field more than two orders of magnitude brighter in the X-ray bands than the other Galactic X-ray emitters: we discuss this interesting source further in § 6.3.

At faint, hard X-ray fluxes, a population of sources appears which are X-ray *overluminous* for their optical magnitudes. They potentially represent an astronomically interesting new population. Unfortunately, most are extremely faint optically and lack spectroscopic identification. Extremely high-redshift ($z \gtrsim 5$) AGN might have bright X-ray fluxes but faint R -band fluxes due to absorption from the Lyman transitions of hydrogen along our line of sight. Obscured AGN, for which high column density absorption near the central black hole shields both the broad-line region and soft X-ray emission, might also be overluminous in the hard X-ray relative to their optical magnitudes. Several examples of these *Type II quasars* have now been identified in the deepest *Chandra* surveys (e.g., Norman et al. 2001; Dawson et al. 2001).

5. Spectroscopic Observations

To date, the SPICES survey has obtained spectroscopic redshifts for 219 of the 485 $K_s < 20$ sources in the Lynx field. This work started in February 1997 and has all been done in multislit mode with the Low Resolution Imaging Spectrometer (LRIS; Oke et al. 1995) on the Keck telescopes. Observations typically used the 150 lines mm^{-1} grating ($\lambda_{\text{blaze}} = 7500 \text{ \AA}$; $\Delta\lambda_{\text{FWHM}} \approx 17 \text{ \AA}$) and sample the wavelength range 4000 \AA to $1\mu\text{m}$. Typical slitlet lengths were $\approx 20''$ and we performed $\approx 3''$ spatial offsets between each 1200 s – 1800 s exposure in order to facilitate removal of fringing at long wavelength ($\lambda \gtrsim 7200 \text{ \AA}$). Masks were designed to contain sources of comparable I -band magnitudes. For the masks containing the brightest sources, two 1200 s exposures were sufficient to obtain redshifts for most sources on the mask. For the masks containing the faintest sources, five 1800 s exposures were not uncommon and some sources have been on multiple faint source masks so that they now have $\gtrsim 10$ hr of spectroscopic integration.

Our infrared selection led to the unintentional spectroscopic targeting of a handful of X-ray sources prior to our obtaining the *Chandra* map. On UT 2000 October 01 we observed a mask dedicated to bright *Chandra* sources for 2400 s in photometric conditions. In total, we have spectroscopic redshifts for 18 of the Lynx *Chandra* sources currently. Table 3 summarizes the spectroscopic results and Fig. 11 presents the spectra. Fig. 12 shows the histogram of redshifts for spectroscopically-identified X-ray sources in this field.

All data reductions were performed using IRAF and followed standard slit spectroscopy procedures. We calculated the pixel-to-wavelength transformation using a NeAr lamp spectrum, generally observed immediately subsequent to the science observations (RMS variations of 0.6 \AA are typical for the 150 lines mm^{-1} grating), and employed telluric emission lines to adjust the wavelength zero-point. The spectra on photometric nights were flux-calibrated using observations of standard stars from Massey & Gronwall (1990).

Consistent with previous spectroscopic studies of faint X-ray hosts (e.g., Fiore et al. 2000; Barger et al. 2001; Giacconi et al. 2001), the Lynx *Chandra* sources are associated with a wide range of astronomical objects. We find two Galactic dwarfs, seven obvious AGN, and nine apparently normal galaxies. Of the galaxies, four are early-type and five show evidence of star formation.

6. Discussion

6.1. Luminosities and Spectral Classification

Table 3 presents the optical and X-ray luminosities for the sample of sources for which we have spectroscopic redshifts. Luminosities have been calculated for two cosmologies: an Einstein-de Sitter (EdS) universe with $H_0 = 50 \text{ km s}^{-1} \text{ Mpc}^{-1}$, consistent with previous work in this field (e.g., Tozzi et al. 2001) and the dark energy (Λ) universe favored by recent supernovae and microwave background observations (e.g., Riess et al. 2001).

We calculate rest-frame B -band luminosities M_B by interpolating rest-frame 4400 Å apparent AB magnitude, $m_{AB}(4400)$, from our broad-band imaging. Magnitudes in the AB system (Oke 1974) are defined by $m_{AB}(\lambda) \equiv -2.5 \log f_\nu(\lambda) + 23.90$, where f_ν is measured in μJy . For the quasar CXO50, our highest-redshift source, we do not have an imaging data point long-ward of rest-frame 4400 Å: for this source we instead assume a standard quasar optical spectral index, $f_\nu \propto \nu^{-0.5}$ (e.g., Richstone & Schmidt 1980; Schneider et al. 1992) and interpolate the flux density from the I -band magnitude. A cosmology-dependent luminosity distance is used to relate apparent magnitude m_{AB} to absolute magnitude M_{AB} , and the same optical spectral index is used to calculate the offset between Vega-based M_B and AB-system $M_{AB}(4400)$: $M_B = M_{AB}(4400) + 0.12$ (e.g., Kennefick, Djorgovski, & de Calvalho 1995). As seen in Table 3, the differences in absolute magnitude are not large between the two cosmologies considered, $M_B^\Lambda = M_B^{\text{EdS}} \pm 0.3$. For the figures below we plot only the Einstein-de Sitter values.

For $\Omega = 1$ and $\Lambda = 0$, the luminosity in the rest frame energy band $E_1 - E_2$, $L_{E_1-E_2}$, is then related to the flux observed in that same energy band, $S_{E_1-E_2}$, by

$$L_{E_1-E_2} = 4\pi \left(\frac{2c}{H_0} \right)^2 \frac{(1+z - \sqrt{1+z})^2}{(1+z)^{2-\Gamma}} S_{E_1-E_2}$$

(e.g., see Hogg 1999), where we adopt an X-ray spectral index $\Gamma = 1.4$ for our sample. Fig. 13 plots the X-ray luminosity of our spectroscopic sample against the rest-frame B -band luminosity, M_B . Fig. 14 plots X-ray luminosity against redshift for our sample, fortified with the HDF-N *Chandra* sources from Hornschemeier et al. (2001). We have recalculated their luminosities for our cosmology and $\Gamma = 1.4$.

We have classified the optical spectra in three broad categories: AGN, galaxies, and stars, following a scheme similar to that of Schmidt et al. (1998) and Hornschemeier et al. (2001). A description of the categories follows:

- **AGN:** We classify sources as AGN that have either (1) broadened emission lines (FWHM $\gtrsim 1000 \text{ km s}^{-1}$) or (2) high-ionization state emission lines such as [Ne V]. Unfortunately the coarse spectral resolution at which many of these data were taken hinders us from separating broad-lined AGN from narrow-lined AGN. Seven of the eighteen sources in the current sample are classified as AGN. They are predominately identified with the most X-ray-luminous sources, $L_X \gtrsim 10^{43} \text{ erg s}^{-1}$. Many are also luminous at optical wavelengths (Fig. 13).
- **Emission-Line and Early-Type Galaxies:** Extragalactic sources without obvious AGN features in their optical spectra are classified as galaxies, though this does not rule out the presence of an active nucleus. We distinguish between galaxies showing emission lines and early-type galaxies, where the latter have redder continua marked by continuum breaks at 2640 Å (B2640), 2900 Å (B2900), and 4000 Å (D4000). Many of the emission-line galaxies show early-type features as well. Nine of the eighteen sources in the current sample are classified as galaxies. For the lower X-ray luminosity sources, stellar processes such as binaries,

winds, and supernovae can produce the X-ray emission. For the higher X-ray luminosity sources, a buried active nucleus is likely present (see §6.4).

- **Stars:** Two of the eighteen sources in the current sample are classified as low-mass Galactic dwarfs. Hornschemeier et al. (2001) also report two X-ray-emitting M4 dwarfs in the *Chandra* field encompassing the HDF-N.

6.2. Notes on Individual Sources

CXO39 ($z = 0.573$, AGN): This X-ray-luminous ($L_{0.5-2} = 10^{43.7}$ ergs s $^{-1}$, $L_{2-10} = 10^{43.8}$ ergs s $^{-1}$) source shows many high equivalent width emission features with deconvolved velocity widths FWHM ≈ 2000 km s $^{-1}$. High-ionization species of Ne are also detected. The spectra were taken without an order-blocking filter, making the continuum unreliable long-ward of 7000 Å.

CXO40 ($z = 0.622$, emission-line galaxy): This galaxy shows a spectrum typical of young, star-forming galaxies: emission from [O II] $\lambda 3727$, the [O III] $\lambda 5007$ doublet, and absorptions from both CaH+K and the hydrogen Balmer lines. The X-ray luminosity is approximately an order of magnitude lower than that typical of sources with obvious AGN features in their optical spectra ($L_{0.5-2} = 10^{42.2}$ ergs s $^{-1}$, $L_{2-10} = 10^{42.4}$ ergs s $^{-1}$), though this does not rule out some fraction of the X-ray emission deriving from a nuclear supermassive black hole.

CXO41 ($z = 1.329$, AGN): This source shows broad Mg II $\lambda 2800$ (FWHM ~ 2500 km s $^{-1}$) and [O II] $\lambda 3727$ emission. The optical spectrum long-ward of 7000 Å is suggestive of a normal star-forming galaxy, a higher redshift analog of CXO40. However, the broad Mg II $\lambda 2800$, high X-ray luminosity ($L_{2-10} = 10^{43.6}$ ergs s $^{-1}$), and strong core in the *HST* image conclusively show that an AGN plays a prominent role in this galaxy.

CXO42 ($z = 1.035$, AGN): This source shows broad Mg II $\lambda 2800$ emission (FWHM ≈ 5300 km s $^{-1}$) and narrow emission lines from high-ionization species of Ne. The [Ne V] $\lambda\lambda 3346, 3426$ lines are individually unresolved at our coarse spectral resolution (FWHM $\lesssim 1300$ km s $^{-1}$). No stellar features are seen. We classify the source as an AGN. The *HST* image shows the source to be unresolved.

CXO44 ($z = 0.725$, emission-line galaxy): The optical spectrum of this source shows weak, spectrally unresolved [O II] $\lambda 3727$ emission superposed on an early-type galaxy spectrum. No obvious AGN features are evident in the optical spectrum. The galaxy is moderately X-ray luminous ($L_{0.5-2} = 10^{42.0}$ ergs s $^{-1}$, $L_{2-10} = 10^{42.9}$ ergs s $^{-1}$). The *HST* image shows a complicated, merging system, suggestive of merger-induced (nuclear?) activity powering the X-ray emission in this system.

CXO49 ($z = 1.017$, emission-line galaxy): This source shows a single emission line straddled by a faint, blue continuum. The most likely identification of such a line is [O II] $\lambda 3727$ (e.g., Stern et al. 2000). The morphology from *HST* image shows an unresolved source.

CXO50 ($z = 3.093$, AGN): This broad-lined AGN is the highest-redshift source in the current sample. It shows the classic features of a broad absorption line quasar (BALQSO). Note that the absorption blue-ward of C III] $\lambda 1909$ is telluric in origin, from the atmospheric A-band.

CXO54 ($z = 0.569$, AGN): This source is similar to CXO41 and CXO42, showing broad Mg II $\lambda 2800$ (FWHM $\sim 6300 \text{ km s}^{-1}$) and narrow [O II] $\lambda 3727$ emission. The [O II] strength is considerably weaker in this source compared to CXO41. We also detect [Ne III] $\lambda 3869$ emission from this source. The redshift places this source at the same redshift of the $z = 0.570$ cluster.

CXO57 ($z = 1.194$, AGN): Similar to many of the other galaxies, this source shows broad Mg II $\lambda 2800$ (FWHM $\sim 6600 \text{ km s}^{-1}$) and strong, narrow [O II] $\lambda 3727$ emission.

CXO63 ($z = 0.899$, AGN): This source shows strong Mg II $\lambda 2800$ and $H\beta$ emission of moderate width, FWHM $\approx 2000 \text{ km s}^{-1}$. Emission from C II] $\lambda 2326$ and [Ne IV] $\lambda 2424$ are also detected. Again, the spectra were taken without an order-blocking filter, making the continuum unreliable long-ward of 7000 \AA .

CXO65 ($z = 0.747$, emission-line galaxy): This source shows an unremarkable galaxy spectrum with a prominent 4000 \AA break (D4000) and unresolved [O II] $\lambda 3727$ emission. No Mg II $\lambda 2800$ emission is detected. The source is moderately X-ray luminous, $L_{0.5-2} = 10^{42.0} \text{ ergs s}^{-1}$ and $L_{2-10} = 10^{42.9} \text{ ergs s}^{-1}$.

CXO66 ($z = 0.336$, emission-line galaxy): This is the least X-ray luminous galaxy in the current spectroscopic sample ($L_{0.5-2} = 10^{41.1} \text{ ergs s}^{-1}$, $L_{2-10} = 10^{42.0} \text{ ergs s}^{-1}$). The spectrum shows classic early-type galaxy features (i.e., Ca H+K absorption, D4000, $H\delta$ absorption) with weak [O II] $\lambda 3727$ and [O III] $\lambda 5007$ emission evident.

CXO72 (M7 V): CXO72 has spectral characteristics intermediate between those of late type dwarfs and giants, suggestive of an intermediate gravity object. The spectral energy distribution between 6500 and 9400 \AA and lack of CaH absorption near 6950 \AA are suggestive of an M7 III giant, while the strengths of the K I doublet near 7700 \AA and the Na I feature near 8400 \AA are more suggestive of an M7 V dwarf. We favor the latter interpretation as it provides a more realistic distance for a low-extinction, high Galactic latitude source: 700 pc , using the Kirkpatrick & McCarthy (1994) optical absolute magnitude tabulation for late-type dwarfs. Unlike the other Galactic dwarf identified in this paper or the two X-ray-emitting dwarfs discussed in Hornschemeier et al. (2001), we detect hard X-rays from CXO72. As seen in Fig. 10, the soft X-ray-to-optical flux ratio is also quite different than the other X-ray dwarfs. Assuming the dwarf interpretation, the corresponding hard X-ray luminosity is $2 \times 10^{29} \text{ ergs s}^{-1}$. We discuss this source further in §6.3.

CXO128 ($z = 0.542$, early-type galaxy): This galaxy, detected only in the soft X-ray band, has an early-type spectrum lacking any emission features. The Ca H+K absorption doublet, 4000 \AA break (D4000), and G-band are very prominent. The I -band magnitude is approximately L^* for a $z \sim 0.55$ giant elliptical galaxy. The redshift of this source is similar to the group at $z = 0.543$, slightly foreground and south of the $z = 0.570$ cluster (see Holden et al. 2001).

CXO138 ($z = 1.26$, early-type galaxy): This extremely red galaxy ($R - K = 6.05$, $K = 17.90$) has a spectrum similar to that of the old, dead, and red radio galaxy LBDS53W091 (Dunlop et al. 1996; Spinrad et al. 1997 – shown for comparison in Fig. 11): the optical spectrum is devoid of emission lines and shows continuum breaks at rest-frame 2640 Å (B2640), 2900 Å (B2900), and 4000 Å (D4000). These features are seen in *International Ultraviolet Explorer* (IUE) spectra of F-type main-sequence stars (Fanelli et al. 1992), implying this is an old (~ 3 Gyr) galaxy at high-redshift. The redshift matches that of the two high-redshift clusters targeted by the *Chandra* observations. The source, detected in the soft X-ray band near our detection limit, has an X-ray luminosity higher than the other spectroscopically non-active galaxies.

CXO139 (M4 V): This M4 dwarf is detected only in the soft band, similar but slightly fainter than the two M4 dwarfs detected in *Chandra* observations of the field encompassing the HDF-N (Hornschemeier et al. 2001). The X-ray-to-optical flux ratio is similar to those stars. Using optical/near-infrared absolute magnitudes of an M4 V dwarf calculated by Kirkpatrick & McCarthy (1994), we derive a distance of ≈ 420 pc for CXO139. The corresponding X-ray luminosity is $L_{0.5-2} = 6.4 \times 10^{27} \text{ ergs s}^{-1}$. Again, this luminosity is similar to the two soft X-ray-emitting M4 dwarfs reported in Hornschemeier et al. (2001). We discuss X-ray emission from Galactic sources further in §6.3.

CXO164 ($z = 0.750$, early-type galaxy): The spectrum of this source is devoid of emission lines and shows absorption from Ca H+K, a D4000 break, and G-band absorption. The source is detected only in the hard X-ray band, suggesting that the source may harbor an obscured AGN from which no feature is evident in the optical data.

CXO167 ($z = 0.432$, early-type galaxy): Similar to CXO164, CXO167 is detected only in the hard X-ray band and shows an early-type galaxy spectrum in the optical devoid of emission lines. The feature near the redshifted [O III] $\lambda 5007$ line is spurious, the residual from a cosmic ray.

6.3. Galactic X-ray sources

Two of the sources in our sample are spectroscopically identified with late-type Galactic dwarfs. Hornschemeier et al. (2001) also find two M4 dwarfs in their survey of the field encompassing the HDF-N. Three of these four sources are very similar: mid-M dwarfs detected only in the soft X-ray band with $\log(f_X/f_R) \approx -2$. The remaining source, CXO72, is a late-M dwarf, detected out to 7 keV and has $\log(f_X/f_R) \approx 0.5 - 1$. We briefly review X-ray emission from late-type stars followed by a discussion of this intriguing new source.

Phenomenologically, the fraction of stars showing stellar activity is found to increase with lower stellar mass, reaching 100% at spectral type M7, then to decrease such that few objects later than type L5 show activity (Hawley, Gizis, & Reid 1996; Gizis et al. 2000). Physically, the observed activity, seen in the form of elevated H α and/or X-ray emission, is believed to result from collisional heating of ions and electrons along magnetic field lines in stellar chromospheres. For

typical chromosphere temperatures, such stars are only detected in the soft X-ray band. Stars more massive than $\simeq 0.3M_{\odot}$ have both convective and radiative zones which allow the formation of a stable internal dynamo through the $\alpha - \Omega$ mechanism (Parker 1955). More rapidly spinning stars have stronger magnetic fields and thus show enhanced activity. Angular momentum loss from stellar winds causes stars to spin-down as they age, with the more massive stars exhibiting stronger winds and thus spinning down more rapidly. The rise in stellar activity from spectral type K5 to spectral type \approx M9 thus simply tracks the fraction of stars sufficiently young for their given spectral type and associated spin-down rate that the internal dynamo can power stellar activity. For spectral types M7 – M9, the spin-down rate is apparently longer than the Hubble time. This scenario is supported by the observed correlation between activity and rotation rate in late type stars (e.g., Kraft 1967; Basri 1987).

The soft-X-ray emitting M4 dwarfs detected by *Chandra* in the deep surveys is consistent with this scenario. Curiously, however, none of these sources show elevated H α emission. CXO72 is a more unusual source. As seen in Fig. 10, for its optical *R*-band magnitude, this star is much brighter in the soft X-ray than the other Galactic X-ray sources discussed here. Some of the difference is likely due to the redder spectral energy distribution of its later spectral class. However, CXO72 is also detected in the hard X-ray band implying a more energetic energy production mechanism than in the soft-band-only Galactic sources. Rutledge et al. (2000) report the *Chandra* detection of an X-ray flare from the lithium-bearing M9 brown dwarf LP944–40, with *soft* X-ray emission detected for 1–2 hr during a 12.1 hr observation. Unlike that source, the X-ray emission from CXO72 is non-transient (Fig. 15). We posit that CXO72 is most likely associated with a very low mass binary system, among the lowest mass such systems observed, with accretion powering the X-ray emission. Burgasser et al. (2000) recently reported strong H α emission from a T dwarf (methane brown dwarf) discovered in the 2MASS survey. They suggest a close [$a \sim (4 - 20)R_J$] interacting binary system with Roche lobe overflow powering the observed emission. Both the H α emission in the T dwarf system and the X-ray emission in CXO72 are not seen to temporally vary in brightness, again suggesting that flaring is not the source of observed stellar activity. Alternatively, most of the hard X-rays from CXO72 come from the second observing period (see Fig. 15), suggesting that time-variable phenomena could be involved.

6.4. X-Ray Emission from Normal Galaxies

Nine of the X-ray sources discussed here show optical spectra devoid of strong or obvious AGN features. As seen in Fig. 14, these sources tend to lie at low redshift ($z \lesssim 1$) with $L_{0.5-2} \lesssim 10^{42} \text{ ergs s}^{-1}$ and $L_{2-10} \lesssim 10^{43} \text{ ergs s}^{-1}$. Many of the sources are detected in only one X-ray band. Similar sources are reported in Mushotzky et al. (2000), Barger et al. (2001), Hornschemeier et al. (2001), and Tozzi et al. (2001). We briefly review physical processes which might produce such emission.

6.4.1. *Actively Star-Forming Galaxies*

With a typical $L_X/L_{\text{bol}} \sim 10^{-7}$ thought to derive from shocks developing in unsteady wind outflows (Pallavicini et al. 1987), isolated late-type stars are not prodigious X-ray emitters. However, a galaxy with a significant young stellar population will produce soft and hard X-rays from several astrophysical mechanisms, primarily associated with the beginning and end stages of massive star evolution (e.g., see Helfand & Moran 2001). Pre-main sequence stars will emit X-rays in their T Tauri phase (e.g., Koyama et al. 1996). Shocks and hot gas associated with stellar winds, galactic winds, and supernovae will also produce X-ray emission, though the dominant source of hard X-ray emission in a starburst galaxy will be accretion-driven from high-mass X-ray binaries (HMXBs).

From a sample of major Local Group Galaxies and Galactic OB stars within 3 kpc of the Sun, Helfand & Moran (2001) infer a specific 2 – 10 keV X-ray luminosity per O star of $2 - 20 \times 10^{34} \text{ ergs s}^{-1}$. Using the models of Leitherer, Carmelle, & Heckman (1995) we can then relate hard X-ray luminosity to the galaxy star formation rate, SFR . For a Salpeter initial mass function (IMF) with slope 2.35, an upper mass cutoff $100 M_\odot$, and solar metallicity, the models of Leitherer et al. (1995) show that a region producing $1 M_\odot \text{ yr}^{-1}$ for at least 10^7 yr will have 2.5×10^4 O stars. Therefore,

$$SFR = 2 - 20 \times 10^{-40} L_{2-10} M_\odot \text{ yr}^{-1},$$

where the hard X-ray luminosity L_{2-10} is measured in ergs s^{-1} .

All of the galaxies in our sample showing evidence of star formation (i.e., sources classified as emission-line galaxies) are indeed detected in the hard X-ray band, with $L_{2-10} \approx 10^{42} - 10^{43} \text{ ergs s}^{-1}$, implying a wide range of possible star formation rates. However, [O II] $\lambda 3727$ luminosity, $L_{[\text{OII}]}$, also provides a crude estimate of star formation rate (Kennicutt 1992):

$$SFR \approx 5 \times 10^{-41} L_{[\text{OII}]} M_\odot \text{ yr}^{-1},$$

where $L_{[\text{OII}]}$ is measured in units of ergs s^{-1} . For our sample of emission-line galaxies, the SFR derived from the X-ray luminosity is typically more than three orders of magnitude greater than that derived from the [O II] $\lambda 3727$ luminosity. The implication is that a buried AGN is likely producing much of the X-ray emission (see §6.4.3) though dust-enshrouded star formation cannot be ruled out.

6.4.2. *Early-Type Galaxies*

The *Einstein Observatory* found that some early-type galaxies are powerful X-ray emitters, with X-ray luminosities correlated with optical luminosities (Forman, Jones, & Tucker 1985), albeit it with a significant dispersion ($L_X \propto L_B^{1.7-3.0}$; e.g., Brown & Bregman 1998). For the X-ray luminous galaxies, hot ($\sim 10^7 \text{ K}$) interstellar gas lost by stars during normal stellar evolution is

thought responsible for producing the X-ray emission. The gas thermalizes in the galactic potential well and then cools as it flows to the center of the galaxy. The X-ray spectra of these galaxies are dominated by thermal emission at $kT \sim 0.8$ keV. It is thought that the X-ray-faint galaxies have lost much of their interstellar gas through galactic winds or from ram pressure stripping by ambient intercluster or intergroup gas. These X-ray-faint galaxies show a harder X-ray spectral component, $\sim 5 - 10$ keV (Matsumoto et al. 1997), with a very soft (~ 0.2 keV) component. Recent *Chandra* observations of the X-ray-faint elliptical galaxy NGC 4697 resolves most of the soft and hard X-ray emission into point sources, the majority of which are low-mass X-ray binaries (LMXBs; Sarazin, Irwin, & Bregman 2000).

In Fig. 13 we plot rest-frame $0.5 - 2$ keV luminosity, $L_{0.5-2}$, against rest-frame B -band absolute magnitude, M_B , for the spectroscopically-observed *Chandra* sources from our survey. We also plot 34 early-type galaxies observed by *ROSAT* by Brown & Bregman (1998). Their sample comprises the 34 optically-brightest, early-type galaxies from the optically-selected, flux-limited sample of Faber et al. (1989), excluding sources with $|b| < 20^\circ$, dwarfs, and M87, known to contain an X-ray bright AGN. Only two sources in our sample classified as early-type galaxies — CXO128 and CXO138 — are detected in the soft X-ray band. Both reside within portions of the $L_{0.5-2} - M_B$ plot (Fig. 13) consistent with the early-type galaxies studied by Brown & Bregman (1998). Several of the sources classified as having emission-line galaxy spectra also have soft X-ray luminosities consistent with the bright early-type sample. The soft X-ray luminosities for these sources can presumably be explained by hot gas and stellar sources. On the other hand, sources CXO164 and CXO167 are both classified as early-type galaxies from their optical spectra but are detected only in the *hard* X-ray band. The X-ray emission in these two sources presumably is powered by a buried AGN. Interestingly, the two soft-band-only early-type galaxies are at redshifts where the Lynx field has known clusters while the two hard-band-only early-type galaxies are at redshifts lacking large-scale structure in the Lynx field.

6.4.3. Obscured AGN

Unification models of AGN invoke orientation as one of the dominant parameters that affect the observed optical properties of an active nucleus. For each broad-lined quasar whose optical emission is Doppler-boosted along our line of sight, a population of *misdirected* quasars should exist whose AGN optical emission is severely attenuated. Norman et al. (2001) report a clear example of one such source, where the optical spectrum shows strong, narrow-lined emission. The well-studied high-redshift radio galaxies (HzRGs) are the radio-loud component of this population: they also typically only exhibit narrow emission lines (e.g., McCarthy 1993; Stern et al. 1999). Presumably the more centrally-condensed broad-lined region (BLR) of these sources has been obscured while the spatially-extended narrow-lined region (NLR) has not been. These spatial scales are consistent with reverberation mapping studies of AGN. For a less luminous active nucleus, the stellar emission from the galaxy might dominate the optical spectral energy distribution, providing an optical spectrum

devoid of AGN features. The effects of obscuration decrease at high energies, allowing X-ray detection of obscured AGN in apparently normal galaxies.

6.5. Comparison to X-Ray Quiet Galaxies

How do the X-ray-emitting galaxies compare to other galaxy populations? In Fig. 16 we show the K -band brightness of sources from our survey plotted against spectroscopic redshift. High-redshift radio galaxies from several radio surveys are also plotted (see De Breuck et al. 2001, and references therein). At each redshift, HzRGs are the most luminous galaxies known at observed $2\mu\text{m}$ (e.g., see Fig. 10 in De Breuck et al. 2001). Since $2\mu\text{m}$ samples stellar emission from the low-mass stars which dominate the baryon content of a galaxy, this is interpreted as HzRGs being the most massive systems at each cosmic epoch (e.g., Dey 1999, and references therein). In Fig. 16 we also plot 219 redshifts from our followup of $K_s < 20$ sources in the Lynx field of SPICES. As we can see from this figure, the *Chandra* sources are among the brighter $2\mu\text{m}$ sources at each redshift, though they are not as luminous as the HzRGs identified from larger area surveys.

7. Conclusions

We present first results from our deep, 184.7 ks *Chandra* map of the Lynx field. This is the third-deepest X-ray field observed thus far by *Chandra*, exceeded in depth only by the megasecond campaigns in the HDF-N and CDF-S (Hornschemeier et al. 2001; Tozzi et al. 2001). We present a catalog of all 153 unresolved field X-ray sources detected in this survey which will provide essential information on the sources responsible for the soft (0.5 – 2 keV) and hard (2 – 10 keV) X-ray backgrounds. We discuss basic results from the X-ray data alone, showing the fainter X-ray sources predominantly have steeper X-ray spectra. We also present multiband optical and near-IR ($BRIzJK_s$) identifications for the $\simeq 66\%$ of Lynx *Chandra* sources which are within the area studied by SPICES, the K -selected imaging and redshift survey we are pursuing (see Eisenhardt et al. 2001). We find $\sim 40\%$ of the spectroscopically-studied subsample are identified with galaxies showing obvious AGN features (i.e., broad lines and high-ionization emission), $\sim 50\%$ are identified with galaxies showing no obvious AGN features, and 2 ($\sim 10\%$) of the sources are identified with late-type Galactic dwarfs. One Galactic source, CXO72, is unusual, having an M7 spectral classification and an unusually hard X-ray spectrum. We discuss this sparse spectroscopic sample in relation to other recently reported deep *Chandra* fields and briefly review X-ray emission from sources not showing obvious AGN features in their optical spectra. We conclude indirectly that many such sources in our survey must indeed harbor an obscured AGN. The catalogs presented here will prove useful for more complete spectroscopic followup allowing direct comparison to models of the X-ray background and studies of the fraction of massive galaxies harboring active, enshrouded nuclei.

We are indebted to numerous colleagues for stimulating conversation and insight regarding this work. In particular, we thank John Gizis, Davy Kirkpatrick, John Stauffer, Jim Liebert, and Bob Rutledge for their input regarding CXO72, the hard X-ray-emitting, late-type Galactic dwarf. We also thank Fiona Harrison, Peter Mao, David Helfand, and Ed Moran for contributing discussion regarding the whole breadth of this project. We thank Roberto della Ceca for providing us with the hard-band $\log N - \log S$ results from *ASCA*. The authors wish to extend special thanks to those of Hawaiian ancestry on whose sacred mountain we are privileged to be guests. Without their generous hospitality, many of the observations presented herein would not have been possible. The work of DS and PE were carried out at the Jet Propulsion Laboratory, California Institute of Technology, under a contract with NASA. The work of SD was supported by IGPP/LLNL University Collaborative Research Program grant #02–AP–015, and was performed under the auspices of the U.S. Department of Energy by University of California Lawrence Livermore National Laboratory under contract No. W–7405–Eng–48. AD’s research is supported by NOAO which is operated by AURA under cooperative agreement with the NSF. This work has been supported by the following grants: NSF grant AST 95–28536 (HS) and NSF CAREER grant AST 9875448 (RE).

REFERENCES

- Akiyama, M. et al. 2000, ApJ, 532, 700
- Arnaud, K. A. 1996, in *Astronomical Data Analysis Software and Systems V*, ed. J. G. Jacoby & J. Barnes, Vol. 101 (San Francisco: ASP Conference Series), 17
- Barger, A., Cowie, L. L., Mushotzky, R. F., & Richards, E. A. 2001, AJ, submitted, astro-ph/0007175
- Basri, G. 1987, ApJ, 316, 377
- Bertin, E. & Arnouts, S. 1996, A&A, 117, 393
- Brown, B. & Bregman, J. 1998, ApJ, 495, L75
- Burgasser, A. J., Kirkpatrick, J. D., Reid, I. N., Liebert, J., Gizis, J. E., & Brown, M. E. 2000, AJ, 120, 473
- Cowie, L. et al. 2001, ApJ, in press (astro-ph/0102306)
- Dawson, S., Stern, D., Bunker, A. J., Spinrad, H., & Dey, A. 2001, AJ, accepted [astro-ph/0105043]
- De Breuck, C., van Breugel, W., Stanford, S. A., Röttgering, H., Miley, G., & Stern, D. 2001, AJ, submitted
- della Ceca, R., Castelli, G., Braito, V., Cagnoni, I., & Maccacaro, T. 1999, ApJ, 524, 674
- Dey, A. 1999, in *The Most Disant Radio Galaxies*, ed. H. Röttgering, P. N. Best, & M. D. Lehnert (Dordrecht: Kluwer), 19
- Dunlop, J. S., Peacock, J. A., Spinrad, H., Dey, A., Jimenez, R., Stern, D., & Windhorst, R. A. 1996, Nature, 381, 581
- Eisenhardt, P., Elston, R., Stanford, S. A., Stern, D., Wu, K. L., Connolly, A., & Spinrad, H. 2001, AJ, in preparation
- Faber, S. M., Wegner, G., Burstein, D., Davies, R. L., Dressler, A., Lynden-Bell, D., & Terlevich, R. J. 1989, ApJS, 69, 763
- Fanelli, M. N., O’Connell, R. W., Burstein, D., & Wu, C. C. 1992, ApJS, 82, 197
- Fiore, F., La Franca, F., Giommi, P., Elvis, M., Matt, G., Comastri, A., Molendi, S., & Gioia, I. 1999, MNRAS, 306, L55
- Fiore, F., La Franca, F., Vignali, C., Comastri, A., Matt, G., Perola, G. C., Cappi, M., , Elvis, et al., 2000, New Astron., 5, 143
- Forman, W., Jones, C., & Tucker, W. 1985, ApJ, 293, 102

- Fowler, A. M., Gatley, I., Stuart, F., Joyce, R. R., & Probst, R. G. 1988, SPIE, 972, 107
- Freeman, P. E., Kashyap, V., Rosner, R., & Lamb, D.Q. 2002, ApJS, in press
- Giacconi, R. et al. 2001, ApJ, 551, 624
- Giommi, P. et al. 1998, Nucl. Phys. B Proc. Suppl., 69, 591
- Gizis, J. E., Monet, D. G., Reid, I. N., Kirkpatrick, J. D., Liebert, J., & Williams, R. J. 2000, AJ, 120, 1085
- Graham, J. R. & Dey, A. 1996, ApJ, 471, 720
- Hasinger, G., Burg, R., Giacconi, R., Hartner, G., Schmidt, M., Trümper, J., & Zamorani, G. 1993, A&A, 275, 1
- Hasinger, G., Burg, R., Giacconi, R., Schmidt, M., Trümper, J., & Zamorani, G. 1998, A&A, 329, 482
- Hasinger, G. et al. 2001, A&A, 365, 45
- Hawarden, T. G., Leggett, S. K., Letawsky, M. B., Ballantyne, D. R., & Casali, M. M. 2001, MNRAS, 325, 563
- Hawley, S. L., Gizis, J. E., & Reid, I. N. 1996, AJ, 112, 2799
- Helfand, D. J. & Moran, E. C. 2001, ApJ, in press; astro-ph/0103484
- Hogg, D. W. 1999, astro-ph/9905116
- Holden, B., Stanford, S. A., Rosati, P., Tozzi, P., Eisenhardt, P. R. M., & Spinrad, H. 2001, AJ, in press (August)
- Hornschemeier, A. E. et al. 2001, ApJ, in press; astro-ph/0101494
- Ishisaki, Y., Makishima, K., Takahashi, T., Ueda, Y., Ogasaka, Y., & Inoue, H. 1999, ApJ, submitted
- Kauffmann, G. & Charlot, S. 1998, MNRAS, 294, 705
- Kennefick, J. D., Djorgovski, S. G., & de Calvalho, R. R. 1995, AJ, 110, 2553
- Kennicutt, R. 1992, ApJ, 388, 310
- Kirkpatrick, J. D. & McCarthy, D. W. 1994, AJ, 107, 333
- Koyama, K., Hamaguchi, K., Ueno, S., Kobeyashi, N., & Feigelson, E. 1996, PASJ, 48, L87
- Kraft, R. P. 1967, ApJ, 150, 551

- Landolt, A. U. 1992, *AJ*, 104, 340
- Leitherer, C., Carmelle, R., & Heckman, T. M. 1995, *ApJS*, 99, 173
- Lilly, S. J., Fevre, O. L., Hammer, F., & Crampton, D. 1996, *ApJ*, 460, L1
- Marshall, F. et al. 1980, *ApJ*, 235, 4
- Massey, P. & Gronwall, C. 1990, *ApJ*, 358, 344
- Matsumoto, H., Koyama, K., Awiki, H., Tsuru, T., Loewenstein, M., & Matsushita, K. 1997, *ApJ*, 482, 133
- McCarthy, P. J. 1993, *ARA&A*, 31, 639
- Mushotzky, R. F., Cowie, L. L., Barger, A. J., & Arnaud, K. A. 2000, *Nature*, 404, 459
- Nakanishi, K., Akiyama, M., Ohta, K., & Yamada, T. 2000, *ApJ*, 534, 587
- Norman, C. et al. 2001, *ApJ*, submitted, astro-ph/0103198
- Ohta, K., Yamada, T., Nakanishi, K., Ogasaka, Y., Kii, T., & Hayashida, K. 1996, *ApJ*, 458, L57
- Oke, J. B. 1974, *ApJS*, 27, 21
- Oke, J. B. et al. 1995, *PASP*, 107, 375
- Pallavicini, R., Peres, G., Serio, S., Vaiana, G., Golub, L., & Rosner, R. 1987, *ApJ*, 248, 279
- Parker, E. N. 1955, *ApJ*, 122, 293
- Richstone, D. O. & Schmidt, M. 1980, *ApJ*, 235, 361
- Riess, A. G. et al. 2001, *ApJ*, in press; astro-ph/010455
- Rosati, P., della Ceca, R., Burg, R., Norman, C., & Giacconi, R. 1995, *ApJ*, 445, L11
- Rosati, P., della Ceca, R., Norman, C., & Giacconi, R. 1998, *ApJ*, 492, L21
- Rosati, P., Stanford, S. A., Eisenhardt, P. R., Elston, R., Spinrad, H., Stern, D., & Dey, A. 1999, *AJ*, 118, 76
- Rutledge, R., Basri, G., Martín, E. L., & Bildsten, L. 2000, *ApJ*, 538, L141
- Sarazin, C., Irwin, J., & Bregman, J. 2000, *ApJ*, 544, 101
- Schmidt, M., Hasinger, G., Gunn, J., Schneider, D., Burg, R., Giacconi, R., Lehmann, I., MacKenty, J., et al., 1998, *A&A*, 329, 495
- Schneider, D. P., van Gorkom, J. H., Schmidt, M., & Gunn, J. E. 1992, *AJ*, 103, 1451

- Schreier, E. J. et al. 2001, ApJ, in press, astro-ph/0106248
- Spinrad, H., Dey, A., Stern, D., Peacock, J. A., Dunlop, J., Jimenez, R., & Windhorst, R. A. 1997, ApJ, 484, 581
- Stanford, S. A., Elston, R., Eisenhardt, P. R. M., Spinrad, H., Stern, D., & Dey, A. 1997, AJ, 114, 2232
- Stanford, S. A., Holden, B., Rosati, P., Tozzi, P., Borgani, S., Eisenhardt, P. R. M., & Spinrad, H. 2001, ApJ, 552, 504
- Stern, D., Bunker, A. J., Spinrad, H., & Dey, A. 2000, ApJ, 537, 73
- Stern, D., Dey, A., Spinrad, H., Maxfield, L. M., Dickinson, M. E., Schlegel, D., & González, R. A. 1999, AJ, 117, 1122
- Stern, D. et al. 2002, ApJ, submitted
- Tozzi, P. et al. 2001, ApJ, in press (astro-ph/0103014)
- Trauger, S. et al. 1994, ApJ, 435, 3
- Ueda, Y. et al. 1999, ApJ, 518, 656
- van Dokkum, P. G., Stanford, S. A., Holden, B. P., Eisenhardt, P. R., Dickinson, M., & Elston, R. 2001, ApJ, in press
- Vecchi, A., Molendi, S., Guainazzi, M., Fiore, F., & Parmar, A. N. 1999, A&A, 349, 73
- Weisskopf, M. C., O’dell, S. L., & van Speybroeck, L. P. 1996, SPIE, 2805, 2

Fig. 1.— False-color X-ray image of the Lynx field, composed from the *Chandra* data. North is to the top, east is to the left. Red/green/blue maps were composed using the following energy channels: 0.3–1 keV, 1–2 keV, and 2–7 keV. Bluer sources have harder spectral indices. Red circles identify the three diffuse X-ray sources associated with hot gas in distant galaxy clusters. The northern cluster is at $z = 0.57$ (see Holden et al. 2001) while the flanking, southern clusters are at $z \simeq 1.27$ (see Stanford et al. 2001). The outer, white square indicates the area of our deep, optical *BRIz* images and the inner, white square indicates the area of our deep near-infrared *JK_s* images.

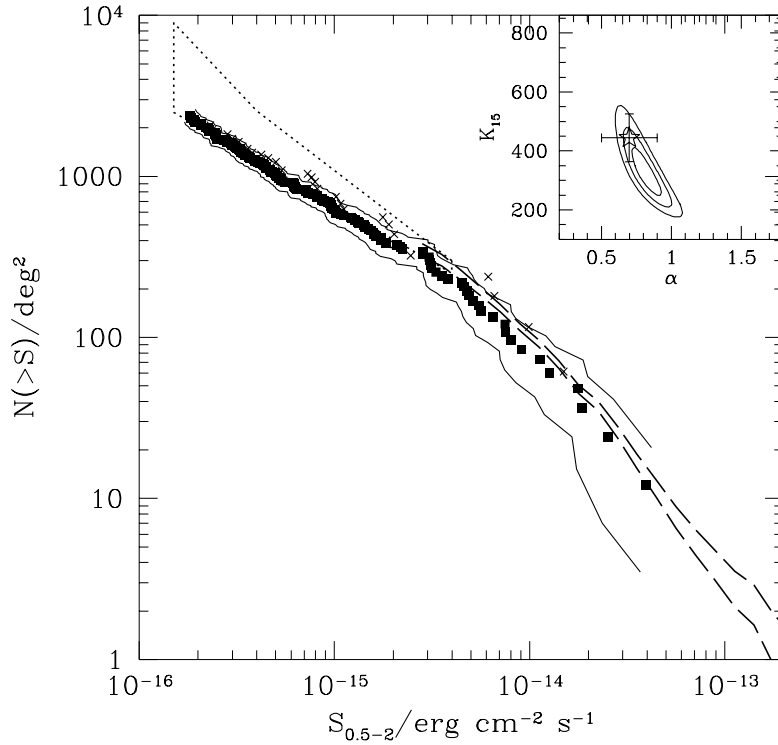


Fig. 2.— The $\log N - \log S$ relation in the soft X-ray band from the deep *Chandra* observations of the Lynx field (filled squares). Crosses are from the 101 ks *Chandra*/ACIS-S3 observations of the SSA13 (Mushotzky et al. 2000). Dashed lines are *ROSAT* counts from the Lockman Hole (Hasinger et al. 1998) and dotted contour is the extrapolation from fluctuation analysis of *ROSAT* data (Hasinger et al. 1993). Insert shows the maximum-likelihood fit to the parameters in the $\log N - \log S$ relation for $N(> S_{0.5-2}) = K_{15}(S_{0.5-2}/2 \times 10^{-15})^{-\alpha}$. The contours correspond to 1σ , 2σ , and 3σ . The star is the fit from Mushotzky et al. (2000) at $S_{0.5-2} = 2 \times 10^{-15} \text{ ergs cm}^{-2} \text{s}^{-1}$, with an error bar corresponding to their 68% confidence limit.

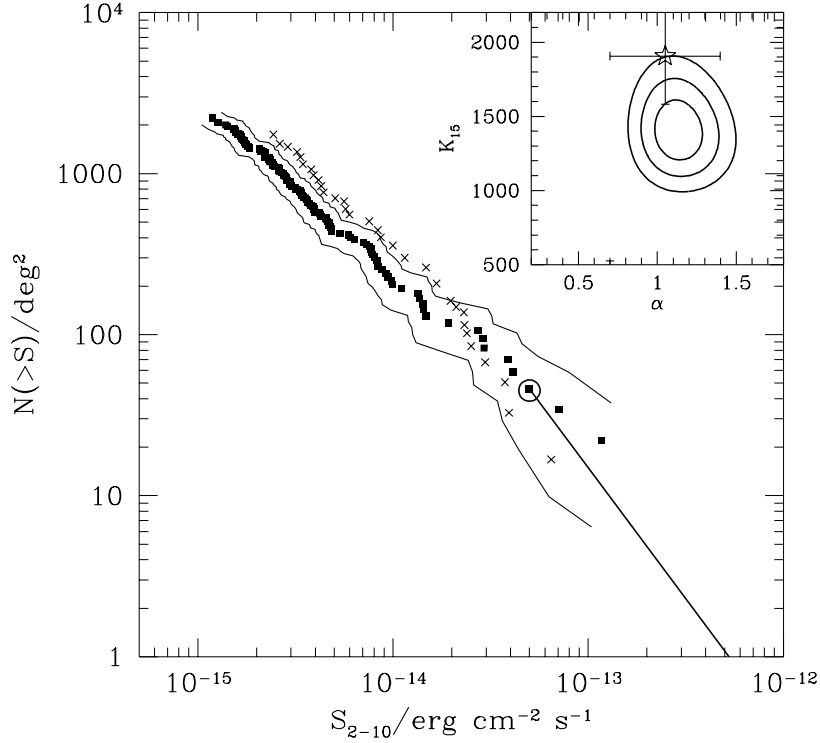


Fig. 3.— The $\log N - \log S$ relation in the hard X-ray band from the deep *Chandra* observations of the Lynx field (filled squares). Crosses are from the 101 ks *Chandra*/ACIS-S3 observations of the SSA13 (Mushotzky et al. 2000). The large open circle at high flux is from *ASCA* and *BeppoSAX* (Giommi et al. 1998, Ueda et al. 1999) and the continuous line is the fit to the *ASCA* counts in the range $(1 - 10) \times 10^{-13}$ ergs cm $^{-2}$ s $^{-1}$ (della Ceca et al. 1999). Upper and lower solid lines indicate uncertainties due to Poisson noise (1σ), calculated for $\Gamma = 1.4$. The insert show the 1, 2, and 3σ maximum likelihood fits to the relation $N(> S_{2-10}) = K_{15}(S_{2-10}/2 \times 10^{-15})^{-\alpha}$. The star shows the results of Mushotzky et al. (2000) at $S = 2 \times 10^{-15}$ ergs cm $^{-2}$ s $^{-1}$, with their 68% confidence limit also illustrated.

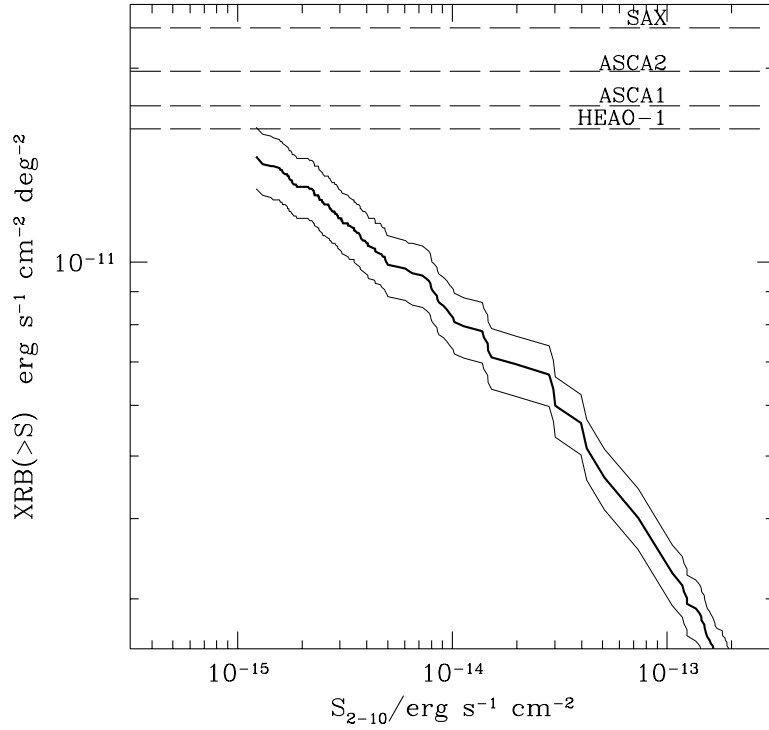


Fig. 4.— Contribution to the hard X-ray background as a function of the flux of resolved sources. For $S_{2-10} < 10^{-13}$ ergs cm $^{-2}$ s $^{-1}$ we show results from the present work. For $S_{2-10} > 10^{-13}$ ergs cm $^{-2}$ s $^{-1}$ we include the contribution derived from the *ASCA* sample of della Ceca et al. (1999). The horizontal lines in the upper part of the plot refer to previous measurements of the hard X-ray background. From bottom to top, they are: Marshall et al. (1980; *HEAO-1*), Ueda et al. (1999; *ASCA1*), Ishisaki et al. (1999; *ASCA2*), and Vecchi et al. (1999; *BeppoSAX*).

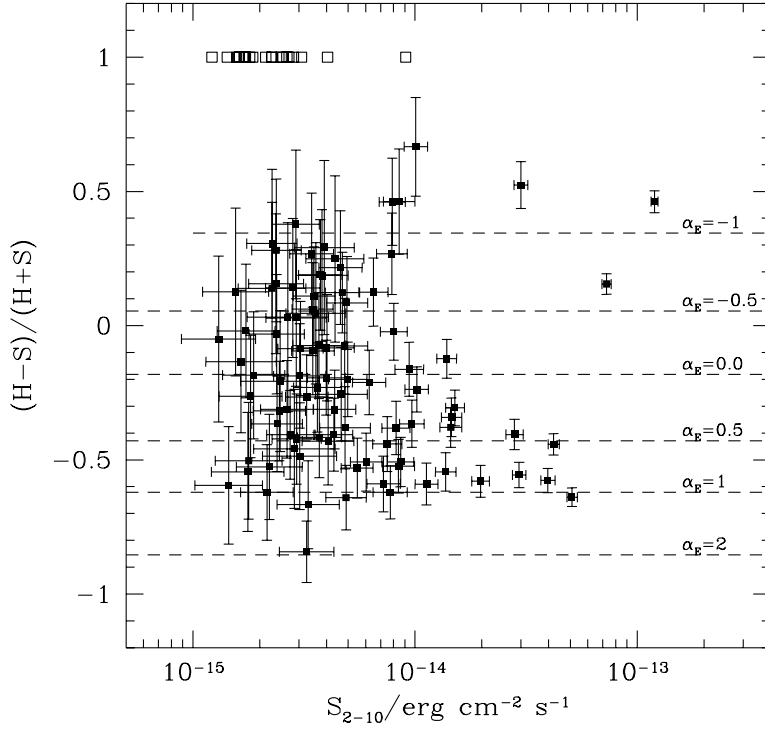


Fig. 5.— Hardness ratio $HR \equiv (H - S)/(H + S)$ of X-ray sources as a function of hard X-ray flux. Sources detected only in the hard X-ray band are shown at a hardness ratio of 1, while sources detected only in the soft X-ray band are not shown. Dashed horizontal lines are power-law models with different energy index ($\alpha_E \equiv \Gamma - 1$) computed assuming the Galactic value $N_H \simeq 2 \times 10^{20} \text{ cm}^{-2}$ and convolved with a mean ACIS response matrix at the aimpoint. The three bright hard X-ray sources with large values of their hardness ratio are, in order of decreasing hard X-ray flux, CXO12 ($HR = 0.46$), CXO37 ($HR = 0.16$), and CXO36 ($HR = 0.53$). Ohta et al. (1996) report that CXO12 is a Type 2 quasar at $z = 0.9$.

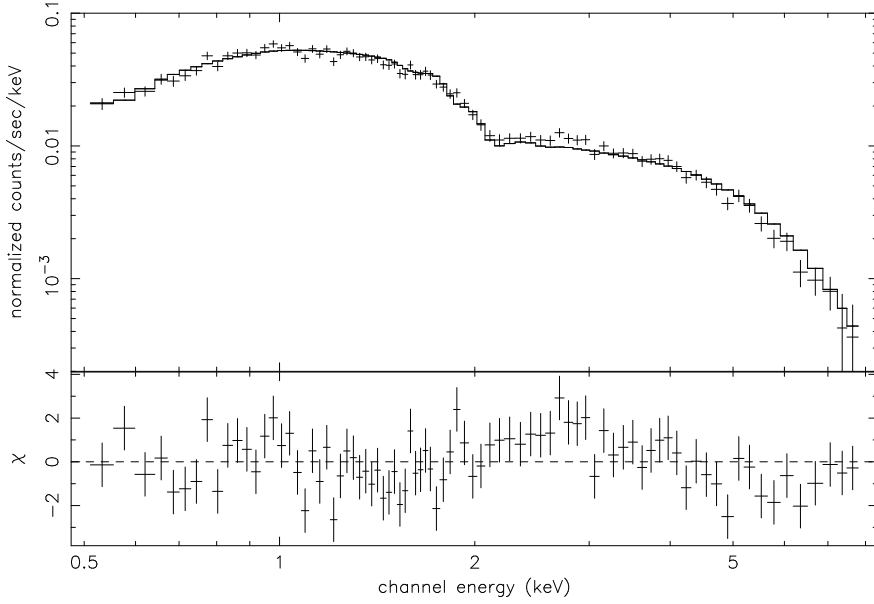


Fig. 6.— Stacked spectrum of the total sample of sources in the Lynx field fitted in the energy band 0.5 – 8 keV with an absorbed power law with variable column density. The best fit slope is $\Gamma = 1.36 \pm 0.04$ and the best fit absorbing column is $N_H = (2.3 \pm 1.4) \times 10^{20} \text{ cm}^{-2}$, consistent with the Galactic value (errors at 90% confidence level). The model, with a $\chi^2_\nu = 1.16$, is in agreement with the average slope of the unresolved hard X-ray background $\langle \Gamma \rangle = 1.4$. The solid line is the best-fit model, while the lower panel shows the standard deviations in each energy bin.

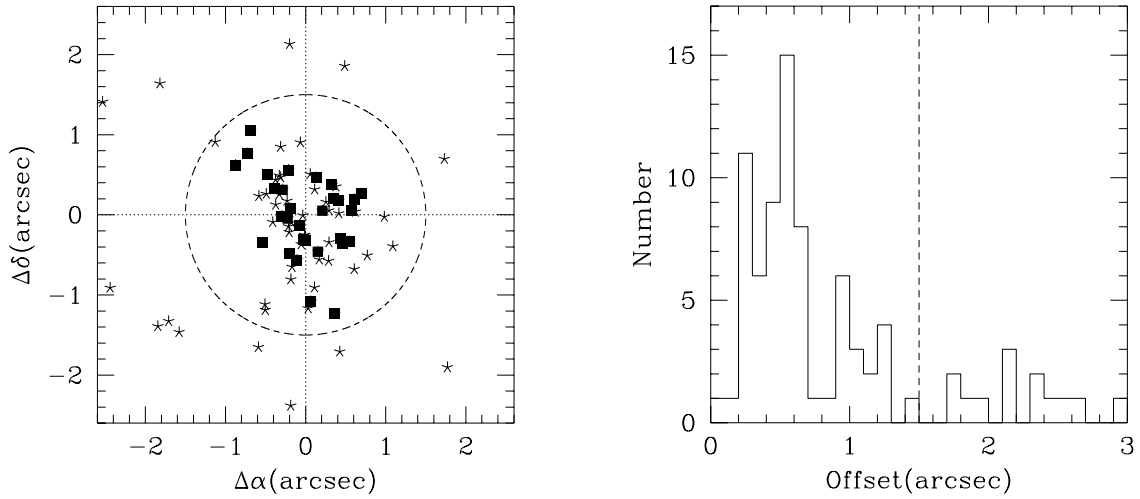


Fig. 7.— Positional offsets between *Chandra* and *I*-band identifications, after aligning the images. Solid boxes in left panel indicate the 30 bright X-ray sources (> 25 counts in the full 0.5–7 keV image) with $17.5 < I < 22.5$ identifications which were used to shift the *Chandra* map to the ground-based imaging. Stars indicate the nearest optical source to each X-ray source, regardless of brightness. We made host identifications using a $1''.5$ matching radius, indicated by the dashed line in both plots.

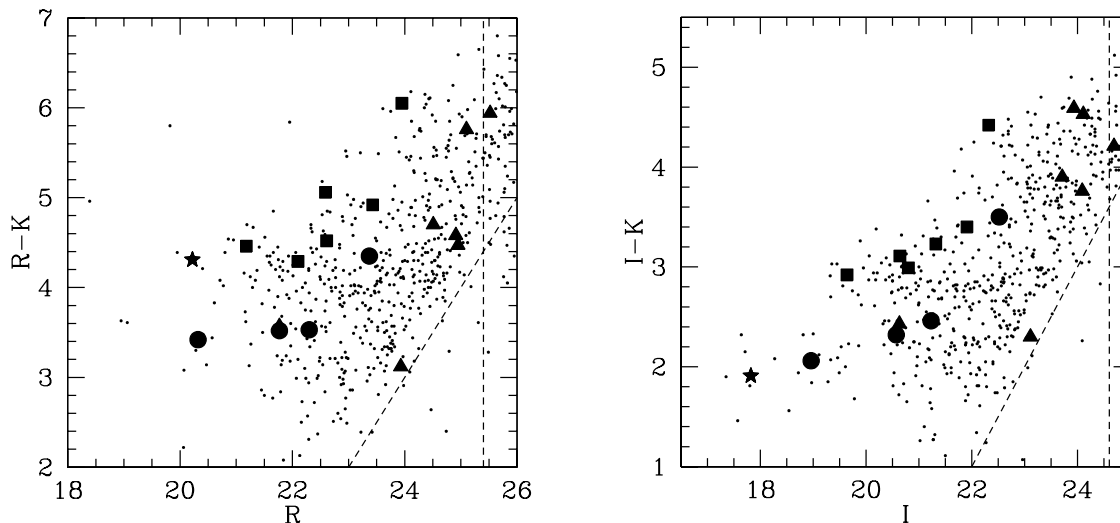


Fig. 8.— Color-magnitude diagrams for sources in the central region of the SPICES Lynx field. Filled symbols represent X-ray sources from this survey: circles are spectroscopically identified with AGN, squares are spectroscopically identified with apparently normal galaxies, the star represents a Galactic M4 V dwarf, and triangles have not been spectroscopically observed as yet. Dots represent field sources from the same region. Dashed lines indicate the limits of our imaging. Note that the bluer sources tend to be associated with AGN, while the redder sources tend to be associated with galaxies.

Fig. 9.— Images of the thirteen *Chandra* sources in the Lynx field which were covered by our *HST*/WFPC2 F702W and F814W pointings. Each panel is $12''$ square centered on the X-ray coordinates, oriented with north to the top and east to the left. Not all sources are detected. The exposure times are 2–10 orbits. CXO52 is a Type 2 quasar at $z = 3.287$, discussed more extensively in Stern et al. (2002).

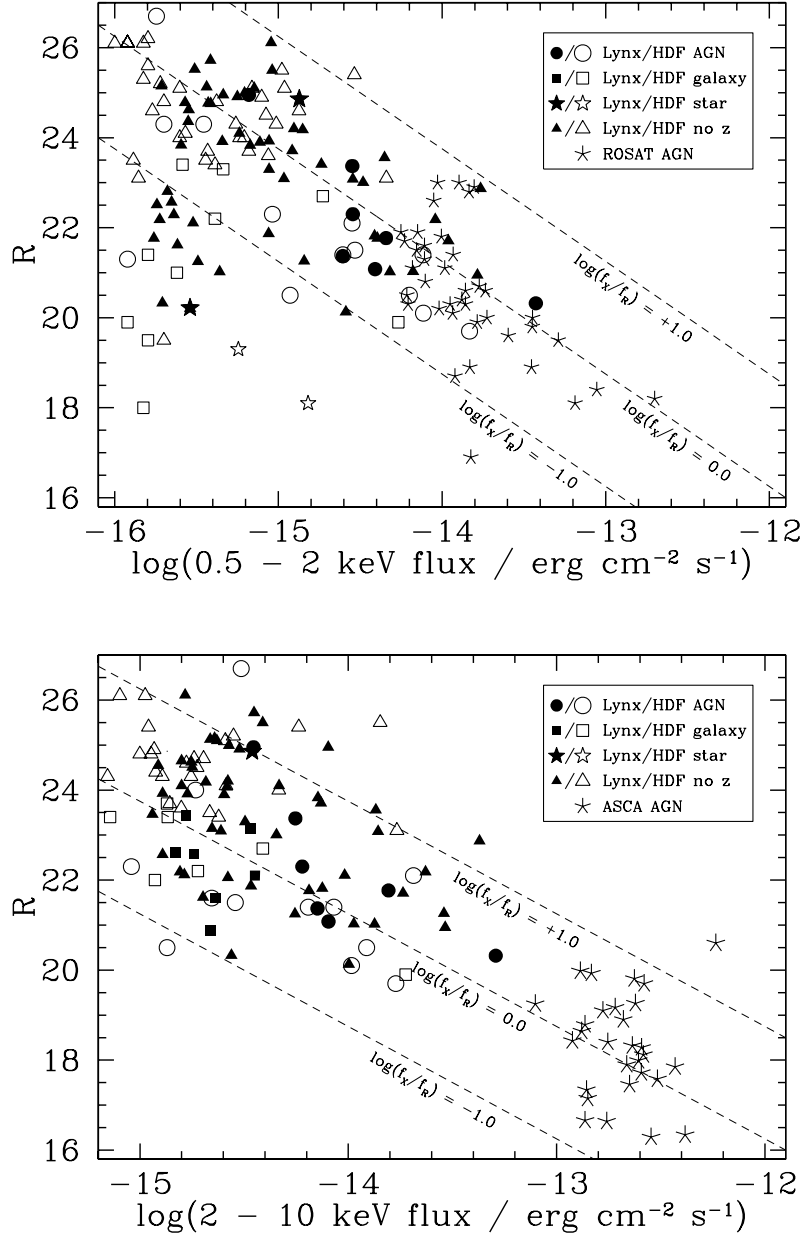


Fig. 10.— Optical R -band magnitude of X-ray selected sources, plotted against soft ($0.5 - 2$ keV) and hard ($2 - 10$ keV) X-ray flux. Filled sources are from the *Chandra* Lynx field presented here. Open sources are from the 221.9 ks *Chandra* survey of the HDF-N reported in Hornschemeier et al. (2001). Asterisks at bright X-ray fluxes show AGN from *ROSAT* for the soft X-ray band (Schmidt et al. 1998) and from *ASCA* for the hard X-ray band (Akiyama et al. 2000). For the *Chandra* surveys, symbol shape corresponds to spectroscopic classification: circles are obvious AGN (i.e., quasars and sources with strong, high-ionization emission lines), squares are apparently-normal galaxies, stars are Galactic dwarfs, and triangles are spectroscopically unidentified sources. We note that the apparently-normal galaxies may harbour low-luminosity and/or heavily-obscured AGN. Slanted lines show location of constant X-ray-to-optical flux ratio.

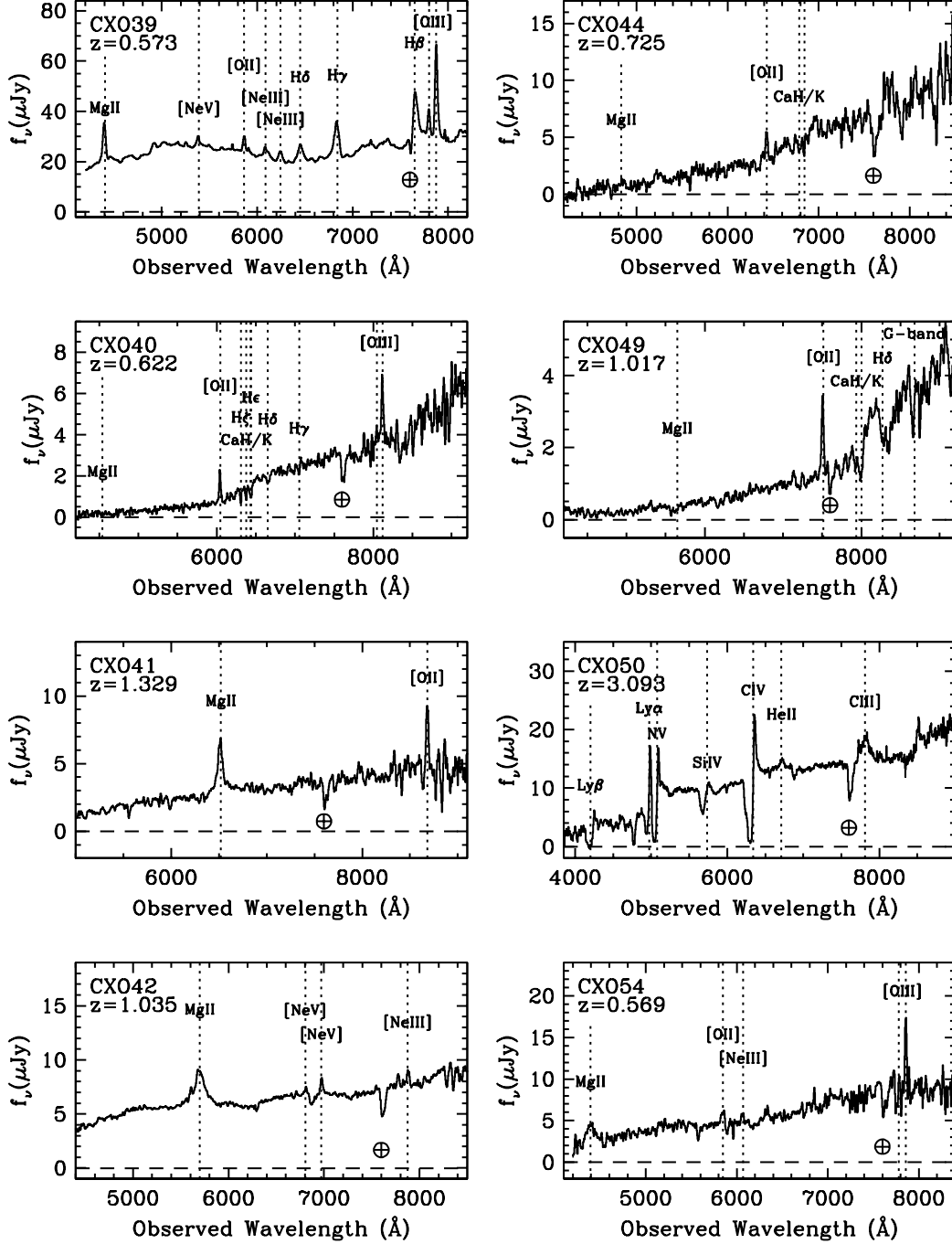


Fig. 11.— Spectra of *Chandra* sources in the Lynx field, obtained with LRIS on the Keck telescopes. Spectra were extracted using $1''.5 \times 1''.5$ apertures and have been smoothed with a boxcar filter, typically of width 15 \AA . Vertical dashed lines indicate the expected wavelength of common spectroscopic features for the spectral class determined in Table 3; not all are detected.

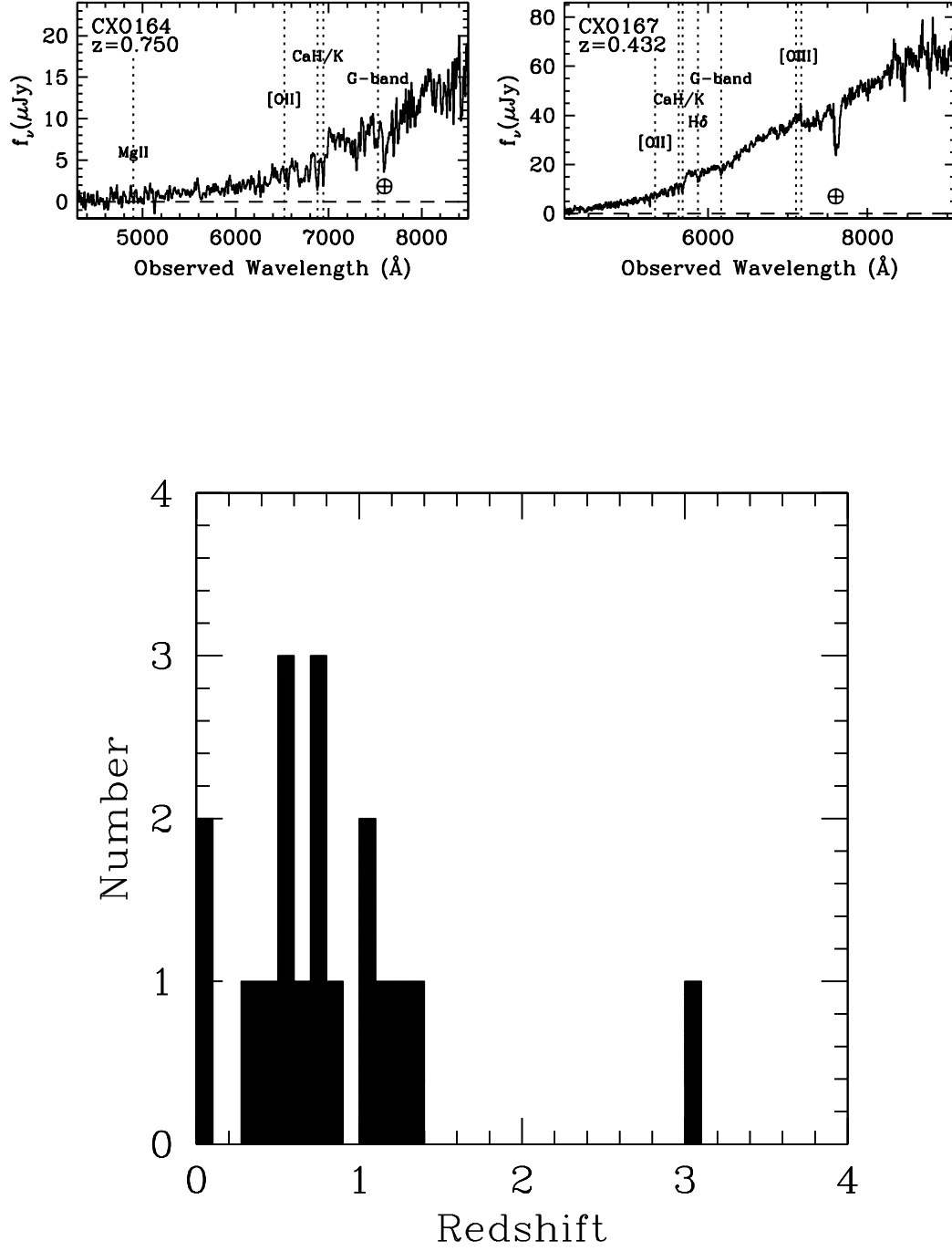


Fig. 12.— Redshift histogram of the 18 *Chandra* sources in the Lynx field for which we reveal spectroscopic information.

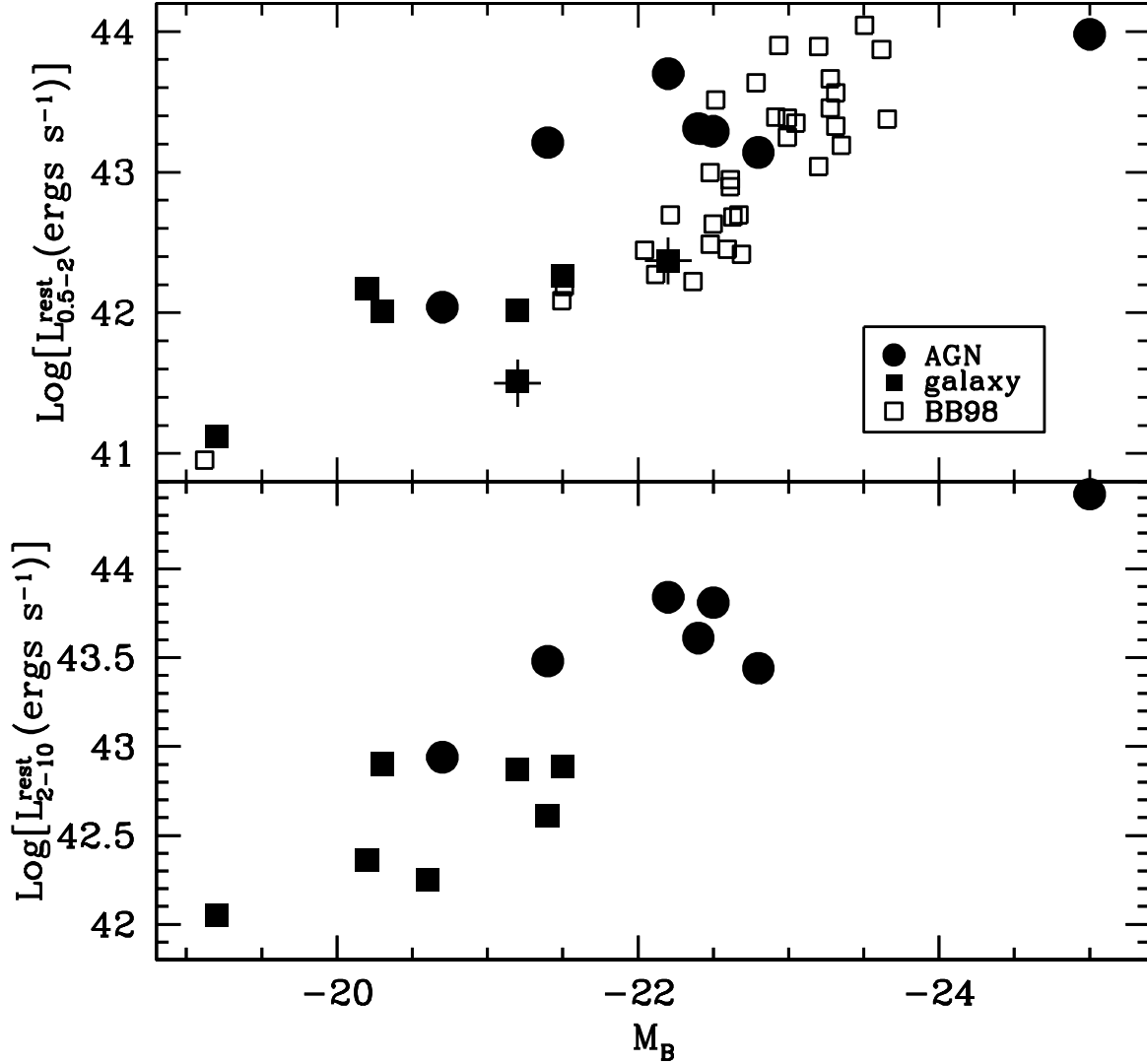


Fig. 13.— X-ray luminosity for the soft ($0.5 - 2$ keV) and hard ($2 - 10$ keV) bands plotted against rest-frame B -band luminosity for the spectroscopic sample discussed here. Symbol shape shows optical spectral classification: solid circles correspond to sources with an AGN obviously present, while solid squares represent optically-normal galaxies. The two early-type galaxies detected in the soft X-ray band (CXO128 and CXO138) are marked with a plus sign in the upper panel. In the upper panel (soft X-ray band), we also include 34 bright early-type galaxies observed by *ROSAT* from Brown & Bregman (1998; BB98), plotted as open squares. See text for details. All symbols are plotted for an Einstein-de Sitter universe with $H_0 = 50 \text{ km s}^{-1} \text{ Mpc}^{-1}$, $\Omega_M = 1$, and $\Omega_\Lambda = 0$. The figure is only slightly changed for the dark energy cosmology favored by recent microwave background and high-redshift supernovae experiments, $H_0 = 65 \text{ km s}^{-1} \text{ Mpc}^{-1}$, $\Omega_M = 0.35$, and $\Omega_\Lambda = 0.65$.

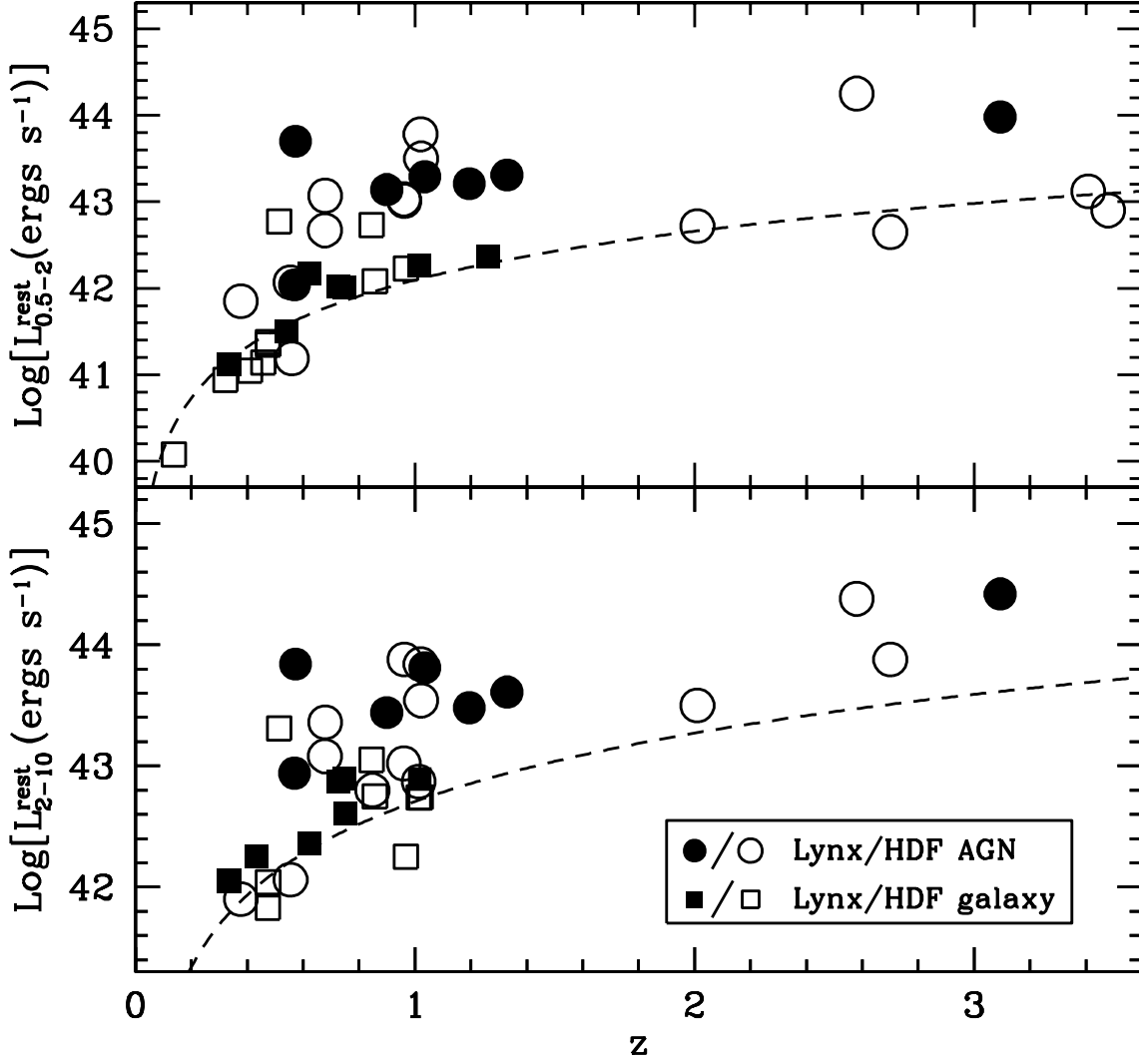


Fig. 14.— X-ray Luminosity for the soft (0.5 – 2 keV) and hard (2 – 10 keV) bands plotted against redshift for two samples of *Chandra* sources. Solid symbols are from this paper. Open symbols are from the HDF-N (Hornschemeier et al. 2001). Luminosities for all sources have been calculated for $\Omega = 1$, $\Lambda = 0$, and $H_0 = 50 \text{ km s}^{-1} \text{ Mpc}^{-1}$, assuming an X-ray spectral index $\Gamma = 1.4$. This entailed recalculating the HDF-N points. We also include the $z = 2.010$ *Chandra* source in the HDF-N recently reported by Dawson et al. (2001). Symbol shape shows optical spectral classification: circles correspond to sources with an AGN obviously present, while squares represent optically-normal galaxies. Dashed lines show the flux limit of our survey: $S_{0.5-2} > 1.7 \times 10^{-16} \text{ ergs cm}^{-2} \text{ s}^{-1}$ and $S_{2-10} > 1.3 \times 10^{-15} \text{ ergs cm}^{-2} \text{ s}^{-1}$. The figure is only slightly changed for the dark energy cosmology favored by recent microwave background and high-redshift supernovae experiments, $H_0 = 65 \text{ km s}^{-1} \text{ Mpc}^{-1}$, $\Omega_M = 0.35$, and $\Omega_\Lambda = 0.65$.

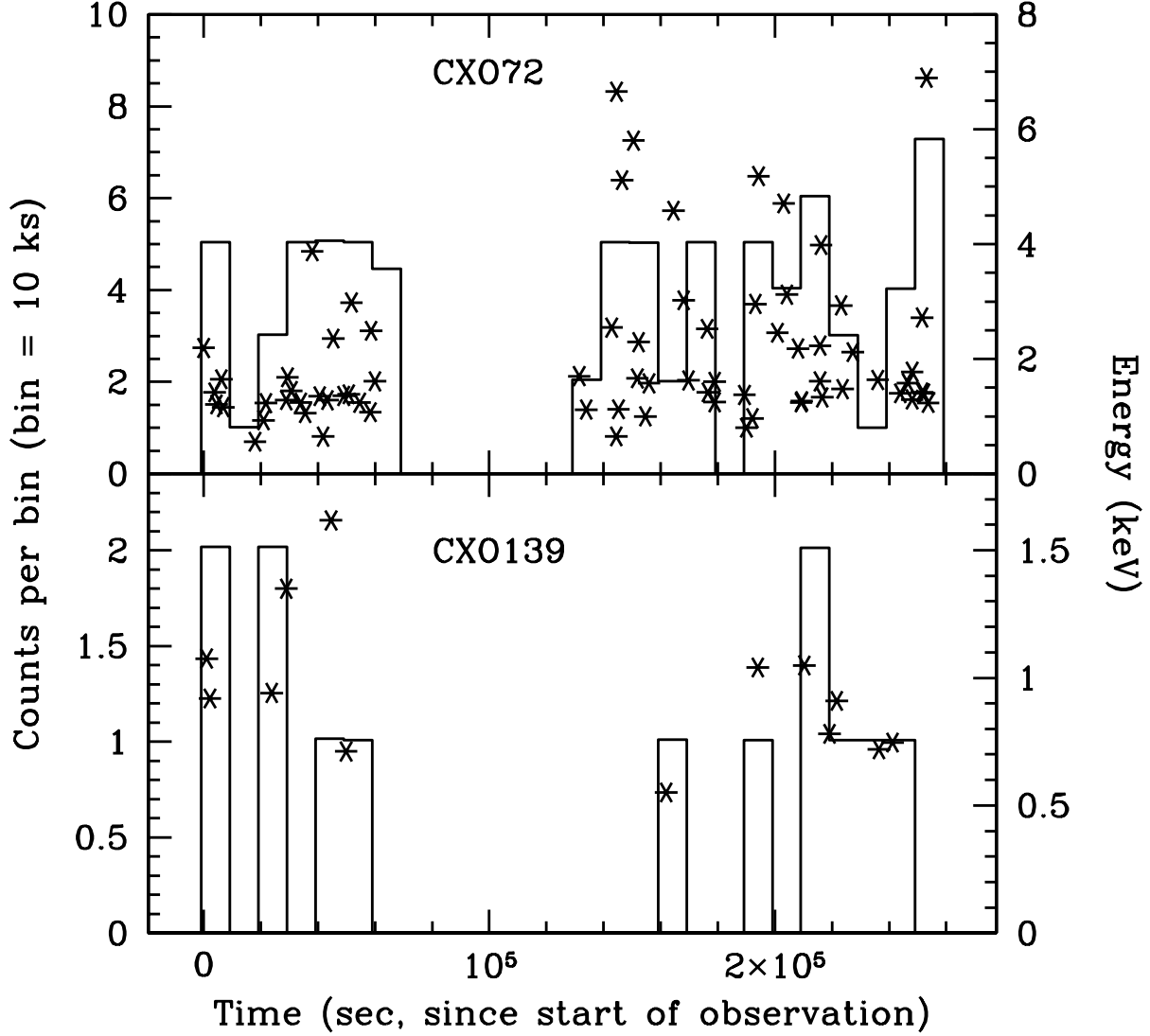


Fig. 15.— X-ray light curves for the two Galactic sources, the M7 dwarf CXO72 and the M4 dwarf CXO139 (histogram; *left-hand scale*). *Chandra* observations of this field were conducted in two campaigns (see §2.1); the gap between these campaigns is clearly evident, centered at 10^6 s after the start of observations. The count rate shows no evidence of variability or flaring for either source. Asterisks mark the times and energies of the each photon detected (*right-hand scale*). The X-ray spectrum of CXO72 appears to steepen over the course of our observations.

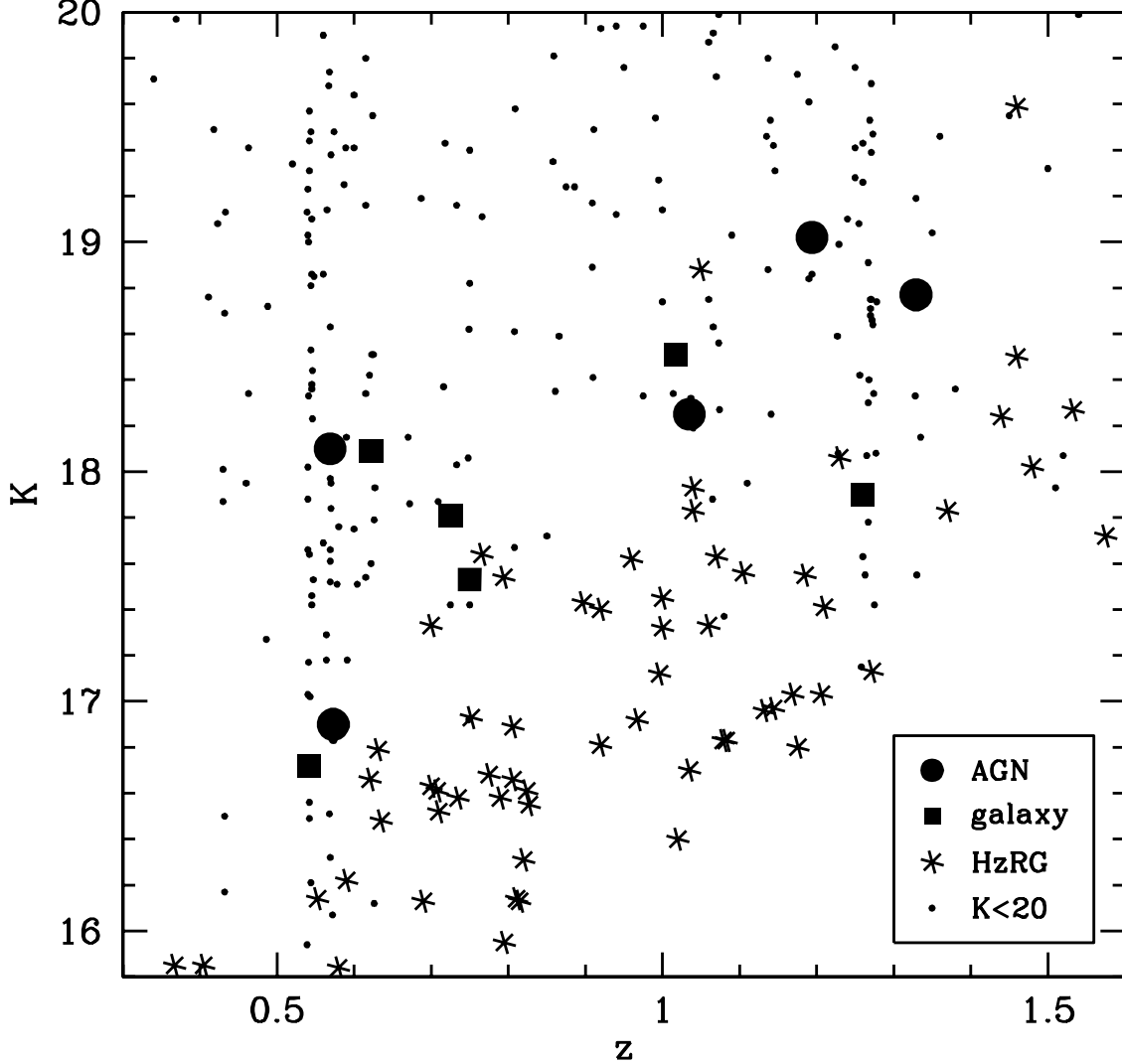


Fig. 16.— K -band brightness plotted against redshift. Larger, solid symbols refer to *Chandra* sources from this paper with symbol shape referring to optical spectral classification: circles refer to obvious AGN while squares refer to optically-normal galaxies. Asterisks are high-redshift radio galaxies (HzRGs) measured in 64 kpc metric diameter apertures ($H_0 = 65 \text{ km s}^{-1} \text{ Mpc}^{-1}$, $\Omega_m = 0.3$, and $\Lambda = 0$) from De Breuck et al. (2001). Dots are galaxies from the Lynx field of the K -selected ($K < 20$) SPICES survey, measured in $3''$ diameter apertures (Eisenhardt et al. 2001). The differing aperture sizes for the samples should produce systematic effects at only a few tenths of a magnitude. Note that the X-ray sources are among the most luminous sources at $2\mu\text{m}$ for each redshift bin. The clusters at $z = 0.57$ and $z = 1.27$ are clearly evident in the field galaxy redshift distribution.

This figure "stern.fig1.gif" is available in "gif" format from:

<http://arXiv.org/ps/astro-ph/0203392v1>

This figure "stern.fig9.gif" is available in "gif" format from:

<http://arXiv.org/ps/astro-ph/0203392v1>

